Layering strategies for active magnetocaloric regenerators using MnFePSi for heat pump applications

Pineda Quijano, Diego; Infante Ferreira, Carlos; Brück, Ekkes

DOI
10.1016/j.applthermaleng.2023.120962

Publication date
2023

Document Version
Final published version

Published in
Applied Thermal Engineering

Applied Thermal Engineering 232 (2023) 120962

Contents lists available at ScienceDirect

Applied Thermal Engineering

journal homepage: www.elsevier.com/locate/apthermeng

Research Paper

Layering strategies for active magnetocaloric regenerators using MnFePSi for heat pump applications

Diego Pineda Quijano [a,b,*], Carlos Infante Ferreira [b], Ekkes Brück [a]

[a] Fundamental Aspects of Materials and Energy, Department of Radiation Science and Technology, TU Delft, Mekelweg 15, 2629 JB Delft, the Netherlands
[b] Process and Energy Laboratory, Delft University of Technology, Leeghwaterstraat 39, 2628 CB, Delft, the Netherlands

ARTICLE INFO

Keywords:
Magnetocaloric heat pump
Layered AMR
MnFePSi
Packed bed
Numerical simulation
Layering strategies

ABSTRACT

The development of affordable magnetocaloric materials (MCM) with a giant magnetocaloric effect (MCE) has brought magnetocaloric heat pumps a step closer to commercialization. The narrow temperature range in which these materials exhibit a large MCE demands the use of several materials with Curie temperatures covering the temperature span of the heat pump in a so-called layered active magnetocaloric regenerator (AMR). How to place these materials in the AMR in terms of distribution of Curie temperatures and thickness of each layer is still a topic of study. In this research we used a one dimensional numerical model to unveil potential benefits of either using a distribution of Curie temperatures that follows a sigmoidal shape or using thicker layers at the cold and hot ends of the AMR along with a linear distribution of Curie temperatures. We found that these AMRs are less sensitive to changes in the hot and cold reservoir temperatures compared to an AMR that uses just a linear distribution of Curie temperatures with uniform layer length, but only the one with thicker ends produces similar heating capacities and second law efficiencies. The heating capacity of the simulated AMR with a sigmoidal distribution of Curie temperatures varies only 5.6 % in a high utilization scenario, flow rate 37.5 g/s and a frequency of 0.75 Hz, when the hot side temperature changes from 308 K to 312 K and the temperature span is 18 K while the corresponding change is 8.7 % for the AMR with thicker end layers, and 37.9 % for the one with a linear distribution of Curie temperatures. For the considered geometry and operating conditions, the maximum heating capacities with temperature span 27 K in the high utilization scenario are 28.6 W, 23.0 W, and 28.5 W, whereas the corresponding second law efficiencies are 33.2%, 27.3 %, and 32.7% for the AMRs with linear distribution of Curie temperatures, sigmoid distribution, and linear distribution with thicker ends respectively.

1. Introduction

The ongoing energy transition urges us to eliminate the use of natural gas and harmful refrigerants for heating and cooling applications. The heat pump market has reacted to this call in two directions: adapting the existing vapour compression technology for the use of natural or environmentally-friendly refrigerants [1], and turning the attention to alternative refrigeration technologies that are still under development [2]. Among the latter, the magnetocaloric heat pumping technology has developed during the last 20 years to the point of having pre-commercial prototypes (see for example references [3,4]) that can be potentially implemented in household refrigerators, air conditioners, and heat pumps and has gained recent attention due to more stringent legislation about the use of refrigerants [5].

Magnetocaloric heat pumps (MCHP) are based on the magnetocaloric effect (MCE), a thermal response that magnetocaloric materials (MCM) exhibit when subjected to a magnetic field change. The MCE can be quantified as an adiabatic temperature change or an isothermal entropy change resulting from the magnetization of the MCM in adiabatic or isothermal conditions respectively. MCHPs consist of three main elements: a magnetic field source, an active magnetocaloric regenerator (AMR), and a hydraulic circuit for the circulation of a heat transfer fluid (HTF). The AMR is the core element of a MCHP and is a porous structure of MCM where magnetic work is converted into heat that is transferred to the HTF. The interested reader can find very detailed information about the principle of operation, thermodynamic cycles, and devices in references [6,7], and [8].

MCHPs can in theory achieve higher efficiencies than traditional vapour compression heat pumps [3,9], and due to the absence of a gas compressor they can also produce less noise, which is an important aspect that limits the widespread utilization of these devices. However,

* Corresponding author.
E-mail address: D.F.PinedaQuijano@tudelft.nl (D. Pineda Quijano).

https://doi.org/10.1016/j.applthermaleng.2023.120962
Received 13 December 2022; Received in revised form 19 May 2023; Accepted 11 June 2023
Available online 15 June 2023

Nomenclature

A	area (m^2)
B	applied magnetic field (T)
c	specific heat capacity (J kg^{-1} K^{-1})
COP	coefficient of performance (-)
d	diameter (m)
DF	degradation factor (-)
f	frequency (Hz)
h	heat transfer coefficient (W m^{-2} K^{-1})
k	thermal conductivity (W m^{-2} K^{-1})
L	length (m)
M	magnetization (A m^2 kg^{-1})
$\dot{m}$	mass flow rate (kg/s)
Nu	Nusselt number (-)
P	pressure (Pa)
Pe	Peclet number (-)
Pr	Prandlt number (-)
$\dot{Q}$	heat transfer rate (W)
$\dot{q}_c$	specific cooling capacity (W kg^{-1})
Re	Reynolds number (-)
s	specific entropy (J kg^{-1} K^{-1})
t	time (s)
T	temperature (K)
T_C	Curie temperature (K)
u_D	superficial velocity (m/s)
U	utilization (-)
V	volume (m^3)
$\dot{V}$	volumetric flow rate (m^3/s)
$\dot{W}$	power (W)
x	distance (m)

Greek symbols

β	specific surface area (m^{-1})
Δ	difference (-)
ϵ	porosity (-)
μ	dynamic viscosity (Pa s)
η	efficiency (-)
ρ	density (kg m^{-3})
τ	cycle period (s)

Subscripts

ad	adiabatic
amb	ambient
AMR	active magnetocaloric regenerator
c	cooling
Carnot	Carnot
cold	cold
cs	cross section
displ	displaced
eff	effective
f	fluid
h	heating
hot	hot
hp	heat pump
m	magnetic
max	maximum
MCE	magnetocaloric effect
p	constant pressure
pump	pump
s	solid
sp	sphere
span	span

Abbreviations

AMR	active magnetocaloric regenerator
EG	ethylene glycol
FWHM	full width half maximum
HTF	heat transfer fluid
MCE	magnetocaloric effect
MCHP	magnetocaloric heat pump
MCM	magnetocaloric material
PBCP	packed bed of crushed particles
PBSP	packed bed of spherical particles
PP	parallel plates
U	utilization

MCHPs are still less competitive than vapour compression heat pumps in terms of cost, which can be attributed to two main aspects. On the one hand side, permanent magnets are the preferred magnetic field source in small to medium capacity MCHPs [6], and these magnets offer a limited magnetic field strength (usually less than 1.6 T is reported [4,10–12], which limits the magnitude of the MCE) and are bulky and expensive. A second aspect that greatly influences the cost of MCHPs concerns the limited frequency and thus limited power density at which they can operate [13], which is primarily restricted by the switching of the valves required to produce an oscillating flow.

Nevertheless, the continuous development of this technology has focused in two main fronts: the development of AMRs and MCHP devices, and the improvement and discovery of MCMs. Engineers have implemented multiple conceptual designs in diverse prototypes all with advantages and disadvantages [7]. Some prototypes are designed as a proof of principle, some other for material testing [11], and a few are developed with an actual application in mind [3,4,14,15]. The former are usually small devices with one or two AMRs, a linear relative movement between AMRs and magnet, and a piston displacer to pump the HTF. The latter are multi-bed devices with a rotating magnet that can achieve cooling capacities of the order of 10^2 to 10^3 W. A few important lessons to consider in the design of a MCHP device are:

- The dead volume can be minimized by installing independent tubing for entering and leaving streams at each side of the AMRs [16].
- The magnetic field in the low field region must be ideally zero or as low as possible in order to maximize the MCE [17]. The duration of the low field part of the cycle must be comparable with the duration of the high field part to allow proper heat exchange between solid and fluid.
- In multi-bed MCHPs, differences in flow resistance between cold-to-hot and hot-to-cold blows in even a single bed cause a flow imbalance that negatively affects the performance of the whole system [18]. This can be controlled by adjusting the time that each bed is open to flow [19].
- In multi-bed devices, using an odd number of AMRs and a two pole magnet helps to reduce the peak torque necessary for the rotation of the magnet [20].
- AMR design must aim to maximize heat transfer between the MCM and HTF while minimizing pressure drop. Thus, an AMR needs a large heat transfer area per unit volume, a large heat transfer coefficient, and a small friction factor [21]. To achieve this, microstructures are potentially the best option [22,23]. Demagnetizing losses also need to be minimized.

On the other hand, material scientists have worked on the search of ideal MCMs that:

Table 1
Summary of Curie temperatures and performance achieved with layered AMRs using second order MCMs tested experimentally.

Ref.	Mat. 1 | $T_{C,1}$ [°C]	Mat. 2 | $T_{C,2}$ [°C]	Mat. 3 | $T_{C,3}$ [°C]	Mat. 4 | $T_{C,4}$ [°C]	T_{cold} [°C]	T_{hot} [°C]	No Load ΔT_{span}	B_{max} [T]	f_{AMR} [Hz]	$\dot{m}_f$ | V_{displ}	HTF
[32]	$Gd_{0.74}Tb_{0.26}$ | 4.8	Gd | 19.8	—	—	3.8	23.8	20.0	2.00	0.80	0.16 g/s	Helium @ 10 atm
[33]	$Gd_{0.85}Er_{0.15}$ | −8.2	$Gd_{0.74}Tb_{0.26}$ | 3.8	Gd | 19.8	—	−21.7	28.3	50.0	2.00	0.80		Helium @ 9.5 atm
[34]	$Gd_{0.85}Er_{0.15}$ | −8.2	Gd | 19.8	—	—	−13.2	31.8	45.0	2.00	0.85	0.33 g/s	Helium @ 9 atm
[36]	$Gd_{0.975}Y_{0.025}$ | 13.0	Gd | 17.0	—	—	1.6	25.0	23.2	1.45	0.50	13.90 cm^3	H_2O/EG (70/30 %V)
[36]	$Gd_{0.95}Y_{0.05}$ | 10.0	Gd | 17.0	—	—	0.1	25.0	24.7	1.45	0.50	13.90 cm^3	H_2O/EG (70/30 %V)
[36]	$Gd_{0.925}Y_{0.075}$ | 4.0	Gd | 17.0	—	—	0.6	25.0	24.2	1.45	0.50	13.90 cm^3	H_2O/EG (70/30 %V)
[35]	$Gd_{0.33}Ho_{0.67}$ | −90.2	$Gd_{0.32}Dy_{0.68}$ | −60.2	$Gd_{0.30}Tb_{0.70}$ | −20.2	Gd | 19.8	−138.2	11.8	150.0	5.00	0.17	3 g/s	Helium @ 27 atm

EG: Ethylene glycol.

- can be synthesized from abundant, non-toxic, and non-radioactive starting elements and compounds [24].
- exhibit a large MCE in low magnetic fields such as the ones produced by permanent magnets. A combination of large adiabatic temperature change and large isothermal entropy change is required to produce a good performance. Having just one of these parameters large and the other small seems to be ineffective [25,26].
- exhibit none or low thermal and magnetic hysteresis. Some MCMs with low thermal hysteresis can still exhibit a reasonably good cyclic adiabatic temperature change [27,28].
- are chemically and mechanically stable to withstand long term cyclic operating conditions. Mechanical stability is in connection with a low or negligible volume change across the phase transition.
- have good mechanical properties to facilitate shaping the MCM into a heat exchanger.
- allow tuning Curie temperature by adjusting the stoichiometry without significantly changing the magnetocaloric properties and the specific heat capacity [29].

Besides Gd, the benchmark MCM for room temperature magnetocaloric refrigeration, and its alloys with Y, Er, Tb, and Ho, all of which are second order MCMs, the $(Mn,Fe)_2(P,Si)$ and the $La(Fe,Si)_{13}$ families of MCMs have also been implemented in magnetocaloric heat pump prototypes, for they have a good combination of properties and can be produced at low cost [30,31]. These two promising MCMs are generally of the first order type (see Lyubina (2017) [29] and Smith et al. (2012) [17] for a clear explanation of differences between first and second order MCMs), which is typically accompanied by a large MCE in a small temperature range and some thermal and magnetic hysteresis. Given the smaller temperature range in which the MCE is expressed, it is necessary to stack several of these MCMs with different Curie temperatures to bridge the temperature span of the heat pump, the so-called layered AMR concept. In the following sections, an overview of experimental and numerical studies with layered AMRs is presented.

1.1. *Experimental studies of layered AMRs using second order MCMs*

First experimental works with layered AMRs focused on AMRs of 2 and 3 layers of uniform length of Gd and Gd alloys [32–34]. Gd and its alloys are second order MCMs, which exhibit the MCE in a wide temperature range, and therefore the separation of Curie temperatures in a layered bed using this type of MCMs can be even as large as 40 K [35]. Table 1 presents a summary of the main characteristics of the layered AMRs used in these initial experimental works as well as some operating parameters and the zero-load temperature span. A few other layered AMRs in which Gd-like materials have been used are also included in Table 1. The initial experiments with layered AMRs proved that it is possible to attain larger zero load temperature spans by adding layers of Gd alloys to the cold side of a pure Gd layer, exploiting the fact that these alloys have Curie temperatures below that of Gd with similar magnetocaloric behaviour. In AMRs of two layers of Gd-like materials, a larger separation of Curie temperatures is generally correlated with a larger zero-load temperature span [32,34]. As in single layer Gd AMRs, it was also shown in these works that ΔT_{span} decreases also approximately linearly with increasing cooling capacity in layered AMRs using Gd-like MCMs. Layered beds can produce however a greater net cooling effect compared to single layer beds when the operating temperatures (cold and hot temperatures) enclose or are nearly above the Curie temperatures of the MCMs used in the bed, but this advantage disappears when the cooling load increases and the temperature span decreases so much that the colder layers operate far from their Curie temperature [36]. So, layered AMRs of Gd-like materials generally produce greater cooling capacities than single Gd AMRs at large temperature spans but poorer cooling capacities at small temperature spans.

Table 2
Summary of Curie temperatures and performance achieved with layered AMRs using first order MCMs tested experimentally.

Ref.	Material family	Geom.	Curie temperature in [°C] (up) and length in [mm] (down) per layer										f_{AMR} [Hz]	V_{max_AMR} [Lpm]	T_{hot} [°C]	B_{max} [T]	$\dot{q}_c$ [W/kg]	ΔT_{span} [K]
			1	2	3	4	5	6	7	8	9	10						
[14]	$La(Fe,Si)_{13}H$	PBSP*	30.5	33.2	36.1	38.6	40.7	43.0	—	—	—	—	4.0	5.30	44	1.44	1375	12.0
			6.3**	6.3	6.3	6.3	6.3	6.3	—	—	—	—						
[37]	$La(Fe,Co,Si)_{13}$	PP	7.8	10.8	18.2	23.8	30.0	35.0	39.0	—	—	—	0.4	0.23	35	1.15	10	12.0
			11.4	11.4	11.4	11.4	11.4	11.4	11.4	—	—	—						
[37]	$La(Fe,Co,Si)_{13}$	PP	18.2	23.8	30.0	35.0	—	—	—	—	—	—	0.4	0.23	35	1.15	10	12.0
			11.4	22.8	22.8	22.8	—	—	—	—	—	—						
[37]	$La(Fe,Co,Si)_{13}$	PP	18.2	23.8	—	—	—	—	—	—	—	—	0.4	0.23	35	1.15	8	12.0
			34.2	45.6	—	—	—	—	—	—	—	—						
[38]	MnFePAs	PBCP	13.8	17.8	21.8	—	—	—	—	—	—	—	0.8	0.62	25	1.45	26	10.0
			14.0	14.0	14.0	—	—	—	—	—	—	—						
[38]	MnFePAs	PBCP	2.2	5.8	8.1	14.5	17.8	22.4	—	—	—	—	0.8	0.61	26	1.45	0+	20.4
			10.0	10.0	10.0	10.0	10.0	10.0	—	—	—	—						
[38]	MnFePAs	PBCP	1.9	5.9	9.7	14.4	18.1	22.2	26.1	29.8	—	—	0.7	0.85	35	1.45	0+	32.0
			15.0	15.0	15.0	15.0	15.0	15.0	15.0	15.0	—	—						
[39]	$La(Fe,Mn,Si)_{13}H_y$	PBCP	17.3	20.6	—	—	—	—	—	—	—	—	0.15	0.04++	30	1.10	0+	13.6
			20.0	20.0	—	—	—	—	—	—	—	—						
[39]	$La(Fe,Mn,Si)_{13}H_y$	PBCP	11.4	13.6	17.5	21.6	26.1	—	—	—	—	—	0.15	0.10++	30	1.10	21	12.0
			8.0	8.0	8.0	8.0	8.0	—	—	—	—	—						
[39]	$La(Fe,Mn,Si)_{13}H_y$	PBCP	11.4	12.3	13.6	15.3	17.5	19.5	21.6	23.7	26.1	—	0.15	0.08++	30	1.10	14	12.0
			4.4	4.4	4.4	4.4	4.4	4.4	4.4	4.4	4.4	—						
[40]	$La(Fe,Mn,Si)_{13}H_y$	PBSP[1]	0.0	2.7	5.3	7.5	9.5	10.7	13.9	15.6	17.0	19.0	1.2	4.55	22	1.44	139	10.0
			28.8	25.0	21.0	19.0	22.5	23.0	28.0	25.5	29.0	40.5						
[41]	MnFePSi	PBCP	19.2	21.5	—	—	—	—	—	—	—	—	1.0	0.33	28	1.47	43	6.0
			22.0	23.0	—	—	—	—	—	—	—	—						
[41]	MnFePSi	PBCP	17.6	21.5	—	—	—	—	—	—	—	—	1.0	0.33	28	1.47	40	5.0
			23.0	23.0	—	—	—	—	—	—	—	—						
[41]	MnFePSi	PBCP	9.9	21.5	—	—	—	—	—	—	—	—	1.0	0.33	37	1.47	39	3.6
			22.0	23.0	—	—	—	—	—	—	—	—						
[41]	MnFePSi	PBCP	8.3	21.5	—	—	—	—	—	—	—	—	1.0	0.33	37	1.47	40	3.6
			22.0	23.0	—	—	—	—	—	—	—	—						
[41]	MnFePSi	PBCP	9.9	19.2	—	—	—	—	—	—	—	—	1.0	0.33	37	1.47	42	3.6
			22.0	22.0	—	—	—	—	—	—	—	—						

PBSP: Packed bed of spherical particles.
PBCP: Packed bed of crushed particles.
PP: Parallel plates.
* The diameter of the spherical particles ranged from 177 to 246 μm.
** Calculated assuming a uniform layer length distribution.
[1] Mass in [g] per layer given instead of length in [mm].
+ Only zero-load temperature span was reported.
++ Calculated from reported utilization values and frequency.

1.2. Experimental studies of layered AMRs using first order MCMs

The discovery of affordable giant MCE materials was followed soon by their implementation in layered AMRs. Table 2 summarizes the main features of some layered AMRs using first order MCMs along with some information regarding the testing device and the resulting performance. As can be seen in Table 2, we focused our attention to layered AMRs based on the Fe_2P and $LaFe_{13}$ families. Compared to Gd, these two families of materials offer larger magnetic entropy change and similar cyclic adiabatic temperature change in a magnetic field change of 0 to 2 T [30]. They can also be produced at low cost, and their starting elements or compounds are widely available [42]. Most AMR prototypes in Table 2 are packed beds of either spherical or crushed particles because shaping these brittle materials into a more structured geometry has proved to be challenging. Generally speaking, single layer Gd AMRs still perform better than most of the layered AMR prototypes presented in Table 2 with the exception of the AMR of Astronautics (reference [14]). The outstanding cooling capacity in this case results from the use of small particle diameters of the order of 200 μm which leads to large heat transfer coefficients (and also large pressure drops reducing thus the system COP), high cycle frequency of 4 Hz in combination with a large flow rate per AMR of 5.3 Lpm, and of course from the use of MCMs with a large and similar MCE under a magnetic field of 1.44 T arranged properly in the AMR.

On the other hand, these experimental studies have also shown that the relation between ΔT_{span} and cooling capacity is not necessarily linear when using first order MCMs in the layered bed [14] as it was also pointed out by Smith et al. [17]. It has also been demonstrated that a large gap in the separation of Curie temperatures between two consecutive layers (e.g. when there is a gap in the full-width-half-maximum of the ΔT_{ad} of two consecutive MCMs in the bed [38]) could lead to having inactive layers above or below the position of the interface between the layers with the large gap [37,41,43]. If it is above or below depends on the operating temperatures. Larger zero load temperature spans are also attainable with layered AMRs whose MCMs have Curie temperatures covering a larger temperature range [38]. Some experimental studies suggest that there is a minimum Curie temperature separation between adjacent layers below which further improvements of performance are marginal. This means that there is a maximum number of layers to cover a certain temperature range after which the performance no longer improves [39]. This is likely related to the fact that the chances that a layer operates far from its Curie temperature increases upon decreasing its length.

1.3. Layering strategies used in experimental studies

Layering strategies depend on two main parameters: the separation of Curie temperature between adjacent layers, and the length of each layer. This second parameter is related to the amount of each material and its position along the AMR. Experimental studies with layered AMRs have typically considered a uniform layer length and a linear distribution of Curie temperatures (see Table 2). In practice some deviation from the intended Curie temperatures is typically present due to the difficulties in the fabrication of MCMs [40], and the final distribution is only approximately linear. On the other hand, a few layered AMRs have been fabricated following different layering strategies.

Masche et al. (2021) tested a new magnetocaloric heat pump prototype with thirteen AMRs of ten layers based on $La(Fe,Mn,Si)_{13}H_y$ MCM [40]. The design of their AMRs considered a linear distribution of Curie temperature. The novelty of their work lies on the filling strategy, for they calculated the length of each layer by considering a constant magnetic energy for each layer along the bed, which was relevant given the tapered shape of the AMRs (in the plane perpendicular to the magnetic field direction) and the variation of the magnetic field along the bed axis. They concluded from numerical simulations that in order to produce a greater cooling capacity this filling strategy is better than other, such as: keeping a constant magnetic flux, using a constant length per layer, or using a constant volume per layer.

Scientists from the AMES Laboratory developed a magnetocaloric methane liquefier using two AMRs of 4 layers consisting of Gd and Gd alloys with Curie temperatures distributed almost linearly from −90.2 °C to 19.8 °C and using helium as HTF (see reference [35]). They used layers of increasing mass from the cold side to the hot side. They claim this is necessary in order to compensate the additional load imposed on hotter layers as these layers have to pump the heat extracted from the cold source plus the magnetic power invested in the colder layers [35].

1.4. Numerical studies with layered AMRs

Numerical simulations facilitate the design and optimization of layered AMRs and have been used to understand the performance of these devices. Lei et al. (2015) performed simulations of layered AMRs based on $La(Fe,Mn,Si)_{13}H_y$ and found that 2.24 layers are necessary for every 5 K of temperature span when the Curie temperatures of the materials are distributed linearly from cold to hot side and the maximum applied magnetic field is 1.2 T [44]. The same group also studied the influence of the number of layers on the performance of layered AMRs. They modelled the magnetocaloric properties of the MCMs using a modified Lorentzian equation [26]. They found that a greater specific cooling capacity is attainable with a smaller number of layers when the peaks of the magnetic entropy change and heat capacity curves are broader. They concluded that there is a maximum number of layers after which the performance of an AMR no longer improves. They also found that the deviations from the Curie temperatures dictated by a linear distribution have a detrimental impact on the performance of layered AMRs. They proposed mixing first and second order MCMs as a method for reducing the sensitivity to the deviations in Curie temperatures. On the other hand, Li et al. (2021) proposed the use of a composite MCM based on a mixture of different compositions of MnFePGe as a way of enlarging the temperature range over which the material exhibits a large magnetic entropy change [45]. However, they did not demonstrate experimentally that such composite material performs as they predicted in an actual AMR. Zhang and co-workers (2017) studied the impact of slightly enlarging 1 or 2 layers of a 16-layer AMR composed of materials of the LaFeMnSiH family, and they found that the simulations in which the coldest layer of the AMR was thicker resulted in an increase in the cooling capacity [46]. Yuan et al. (2022) proposed to use an MCE-length diagram as a guide to optimize the design of layered AMRs [47]. After implementing a genetic algorithm optimization process, they also found that using thicker end layers leads to greater specific cooling powers for temperature spans above the design temperature span. They also suggested that temperature distributions of the solid material along the bed must be included in the analysis of the layering strategy [47]. Risser et al. also used evolutionary algorithms for the optimization of the design of layered AMRs [48]. Monfared and Palm (2015) simulated a 6-layer AMR using Gd-like materials. They considered initially a linear distribution of Curie temperatures and uniform layer length (base case). Then, they created many different AMRs by matching Curie temperatures of new materials with the average temperature of the layers of the base case at many different moments of the cycle [49]. After simulating the new AMRs obtained in this way, they concluded that matching the distribution of Curie temperatures with the solid temperature profile obtained at the end of the magnetization process would produce the highest COP whereas matching it with the profile obtained at a moment near the end of the cold-to-hot blow would produce the largest temperature span.

1.5. Challenges of layered AMRs

A few general challenges of layered AMR are:

- The magnetocaloric properties of the MCMs are difficult to reproduce when applying manufacturing methods needed for massive production. As a result, it is difficult to obtain the exact Curie temperatures required for a particular layered AMR [4].
- It is also difficult to have uniformity of magnetocaloric properties in a layered bed. Typically there are variations in the height and width of the peaks of the specific heat capacity, adiabatic temperature change, and magnetic entropy change from one material to another even if there are only slight changes in their compositions [41].
- Depending on the manufacturing method, each layer can have a different porosity and pore geometry [4]. This is especially difficult to control in packed beds, but it could be controlled using 3D printing techniques.

As the previous literature study suggests, the definition of the layering strategy of layered AMRs, i.e. the definition of the Curie temperature and thickness of each layer, is still a challenging topic of study. This is a critical task when using first order materials with narrow MCE peaks because each material must be placed in a position in the AMR bed whose temperature closely fluctuates around its Curie temperature so that the entire AMR can exhibit a good MCE [21]. To enable this, it is necessary to decrease the utilization factor of the regenerator. This is achievable by increasing the peak specific heat capacity of every MCM in the bed. However, a high specific heat capacity has a detrimental effect on the adiabatic temperature change of MCMs, so a compromise is needed. The utilization factor can also be limited by decreasing the mass flow rate or increasing the cycle frequency, but this will limit the cooling and heating capacity that the AMR can develop.

Nevertheless, as each layer has a finite length, only a portion of the MCM in each layer will actually fluctuate around the optimum temperatures. Because of this, it has been said that a layered AMR should ideally have an infinite number of layers so that it can have a continuous change in Curie temperature [17], but this is impractical using traditional manufacturing methods. Alternatively, researchers from the FAME group at TU Delft have hypothesised that an AMR based on the $(Mn,Fe)_2(P,Si)$ family of compounds could have a continuous change in Curie temperature along its length by 3D printing a regenerator matrix initially consisting of a few compositions and then allowing the diffusion of elements during the heat treatment process to obtain a continuous change in composition and thus also a continuous change in Curie temperatures. Depending on the selected initial compositions, it could be possible to obtain a linear or a sigmoidal distribution of Curie temperatures, or any other arbitrary function in theory. So, a question that immediately comes out is: which distribution of Curie temperature would be more advantageous for the performance of an AMR for a particular MCHP application?.

1.6. Goals of the present study

The previous sub-sections make clear that different studies have concluded differently for what concerns the optimum layering strategy. In this article we compare the performance of three AMRs with different Curie temperature distributions: one following a simple linear function, a second following a sigmoidal function, and a third also following a linear function but using thicker end layers at the same time. For this comparison, we use a one dimensional physical model of an AMR. Because the model equations are solved using numerical methods, a large but finite number of layers are considered to resemble the continuous change in Curie temperatures. The operating temperatures of the AMRs are defined in this article by considering a heat pump application although the findings apply to both refrigeration and heat pump applications. A similar system as the one described by Johra et al. (2019) [50], which makes use of a borehole ground heat exchanger as heat source and an underfloor heating system as heat sink, is considered here for the definition of the operating temperatures of the heat source and heat sink, 281 K and 308 K respectively and thus 27 K temperature span. This is the design temperature span.

2. Methods

2.1. Mathematical model

The influence of different layering strategies on the performance of an AMR was studied with a one-dimensional numerical model of an AMR. The model is based on the implementation of Christiaanse and coworkers, whose details are reported in [51] and is publically available [52]. For the sake of completeness, some necessary information about this model is reproduced here. This model departs from the following basic assumptions, common to many models as pointed out by Nielsen et al. (2011) [53]:

- The fluid remains always in the liquid phase.
- Heat transfer by radiation is negligible.
- The MCM is uniformly distributed in the volume occupied by the AMR.
- The velocity of the fluid is uniform in any cross section of the AMR, i.e. plug flow is assumed.
- The mass flow rate of the fluid entering the AMR is imposed via a mass flow rate vs time profile.
- The applied magnetic field is uniform along the fluid flow direction.

The energy conservation equations for the fluid and solid domains are presented in equations (1) and (2) respectively. As can be read in equation (1) from left to right, thermal energy storage, energy accompanying mass flow, heat conduction, viscous dissipation, heat leaks to ambient, and heat transfer with the solid have been considered in the fluid energy balance. For the solid energy balance of equation (2), thermal energy storage, heat conduction, the magnetocaloric effect modelled as a heat source term and calculated with equation (3), and the heat transfer with the fluid are the physical phenomena considered.

$$\rho_f c_f A_{cs} \epsilon \frac{\partial T_f}{\partial t} + \frac{\partial}{\partial x}\left(\dot{m} c_f T_f\right) - \frac{\partial}{\partial x}\left(k_{f,\mathrm{eff}} A_{cs} \epsilon \frac{\partial T_f}{\partial x}\right) = \left|\frac{\dot{m}}{\rho_f}\frac{\partial P}{\partial x}\right| + \dot{Q}_{\mathrm{amb}} + A_{cs}\beta h\left(T_s - T_f\right) \quad (1)$$

$$\rho_s c_s A_{cs}(1-\epsilon)\frac{\partial T_s}{\partial t} - \frac{\partial}{\partial x}\left(k_{s,\mathrm{eff}} A_{cs}(1-\epsilon)\frac{\partial T_s}{\partial x}\right) = \dot{Q}_{\mathrm{MCE}} + A_{cs}\beta h\left(T_f - T_s\right) \quad (2)$$

$$\dot{Q}_{\mathrm{MCE}} = -\rho_s A_{cs}(1-\epsilon) T_s \left.\frac{\partial s}{\partial B}\right|_{T_s} \frac{\mathrm{d}B}{\mathrm{d}t} \quad (3)$$

Some researchers include the momentum conservation equation in their AMR models, and they solve it uncoupled from the energy conservation equations by considering constant fluid properties independent of temperature and assuming a $\Delta P(t)$ function (see for example 1D models [12,54] and 2D models [55,56]). Then, they use the resulting velocity field in the energy conservation equations presented in (1) and (2). On the other hand, the vast majority of 1D AMR models omit the solution of the momentum equation for the sake of simplicity and derive a velocity field from a mass flow rate vs time profile used as a boundary condition [18,57,58]. These models still produce sufficiently accurate results [59]. Here we opt for the second approach.

In this study we consider that the AMRs are packed beds of spherical particles. Consequently, the following constitutive equations were implemented. The heat transfer coefficient was calculated from the Nusselt correlation shown in equation (4), where the Reynolds number is based on pore velocity and particle diameter. This correlation was

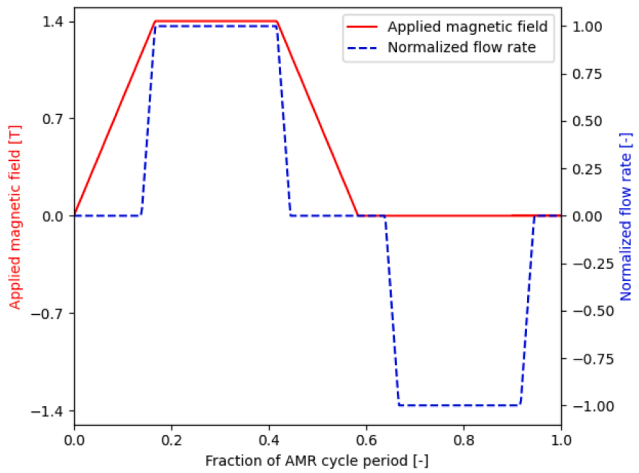

Fig. 1. Fluid flow and magnetic field profiles.

developed by Macias-Machin et al. (1991) [60] and adopted by Park et al. (2013) [61] for an AMR model. Even though this correlation was developed for fluidized beds, it provides smaller heat transfer coefficients in comparison with other correlations typically used in AMR modelling such as Wakao and Kaguei (1982) [62], which usually lead to over prediction of performance as pointed out by Frischmann et al. (2008) [63]. Macias-Machin (1991) gives heat transfer coefficient values that are comparable to the ones resulting from the correlation developed by Frischmann et al. (2008), and it also produces a non-zero Nusselt number when the velocity of the fluid goes to zero, which is advantageous for flow profiles with stagnation periods in the AMR cycle. Temperature gradients inside the spherical particles have been considered by the use of a degradation factor, *DF*, as proposed by Engelbrecht et al. (2006) [64].

$$Nu = 1.27 + 2.66\ Re^{0.56}\ Pr^{-0.41}\left(\frac{1-\epsilon}{\epsilon}\right)^{0.29} \tag{4}$$

$$h = \frac{Nuk_f}{d_{sp}}DF \tag{5}$$

The effect of thermal dispersion in the fluid phase in the direction parallel to the flow is considered by using an effective thermal conductivity, equation (6), where $Pe = Re\ Pr$ with Reynolds number calculated based on particle radius and superficial velocity. On the other hand, the thermal conductivity in the solid phase is corrected to account for the presence of the fluid in between the solid particles by the use of equation (7) proposed by Hadley (1986) [65], where $a_0 = 10^{-1.084-6.778\ (\epsilon-0.298)}$ and $f_0 = 0.8 + 0.1\epsilon$.

$$k_{f,\text{eff}} = k_f\left(1 + \frac{3}{4}Pe\right) \tag{6}$$

$$k_{s,\text{eff}} = k_f\left(\frac{(1-a_0)\left(\epsilon\ f_0 + (1-\epsilon\ f_0)\ \frac{k_s}{k_f}\right)}{1-\epsilon\ (1-f_0) + \epsilon\ (1-f_0)\ \frac{k_s}{k_f}} + a_0\frac{2\ (1-\epsilon)\ \frac{k_s^2}{k_f^2} + (1+2\ \epsilon)\ \frac{k_s}{k_f}}{(2+\epsilon)\ \frac{k_s}{k_f} + 1 - \epsilon}\right) \tag{7}$$

Pressure drop per unit length is calculated with equation (8), also known as Ergun equation [66].

$$\frac{\partial P}{\partial x} = \frac{1.75\ u_D^2\ (1-\epsilon)\ \rho_f}{d_{sp}\ \epsilon^3} + \frac{150\ u_D\ (1-\epsilon)^2\ \mu_f}{d_{sp}^2\ \epsilon^3} \tag{8}$$

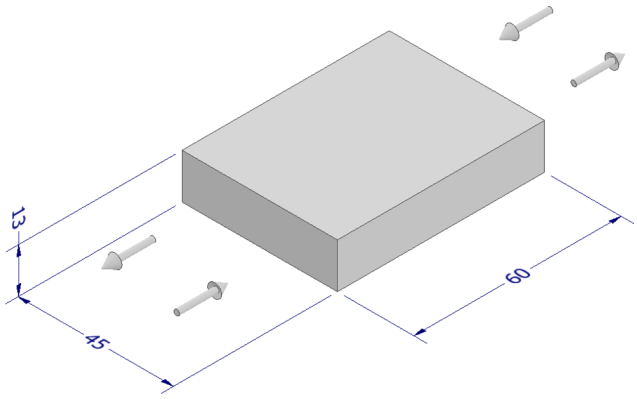

Fig. 2. Overall geometry and dimensions of the AMR (in mm).

Table 3
Parameters used in the simulations.

Parameter	Value	Units
AMR WxHxL	45x13x60	mm × mm × mm
Porosity (ϵ)	0.36	—
Particle diameter (d_{sp})	300	μm
Max. Magnetic field intensity	1.4	T
Frequency AMR	[0.75, 4.50]	Hz
Max. mass flow rates	[25.00, 37.50]	g s^{-1}
T_{amb}	288	K
T_{hot}	[308, 310, 312]	K
$\Delta T_{span} = T_{hot} - T_{cold}$	[18, 21, 24, 27, 30, 33]	K

The energy conservation equations were solved using a finite difference method. The discretization of these equations followed the Crank-Nicholson scheme for the diffusion terms in both equations, and also for the fluid temperature in the heat-leak term, and the solid temperature in the term corresponding to heat transfer by convection. The upwind scheme fully implicit in time was used for the enthalpy term of the fluid energy conservation equation and for the fluid temperature in the term corresponding to heat transfer by convection. A full description of the discretization method can be found in Christiaanse (2018) [67]. The system of linear algebraic equations resulting from the discretization was solved using a three diagonal matrix algorithm. This model was implemented in Python. The validation of this model is presented in reference [51] for the case of two-layer MnFePSi AMRs. We also validated the model using the experimental data of a device with a single packed bed of Gd spheres reported by Trevizoli et al. (2016) [68], and we obtained good agreement.

2.2. Performance metrics

The heating capacity is one of the key performance parameters of a heat pump. It is calculated for the AMR case with equation (9). Likewise, the cooling capacity can be calculated with equation (10). Another important performance parameter is the COP of the heat pump, which is here calculated using equation (11) where $\dot{W}_m$ corresponds to the magnetic power, equation (3). Finally, second law efficiency, defined by equation (12), is used to compare the performance of the AMRs with the theoretical maximum.

$$\dot{Q}_h = f_{AMR}\int_0^{1/f_{AMR}} \dot{m}_f(t)\ c_f\ \left(T_{f_{(x=L,t)}} - T_{hot}\right)\ dt \tag{9}$$

$$\dot{Q}_c = f_{AMR}\int_0^{1/f_{AMR}} \dot{m}_f(t)\ c_f\ \left(T_{cold} - T_{f_{(x=0,t)}}\right)\ dt \tag{10}$$

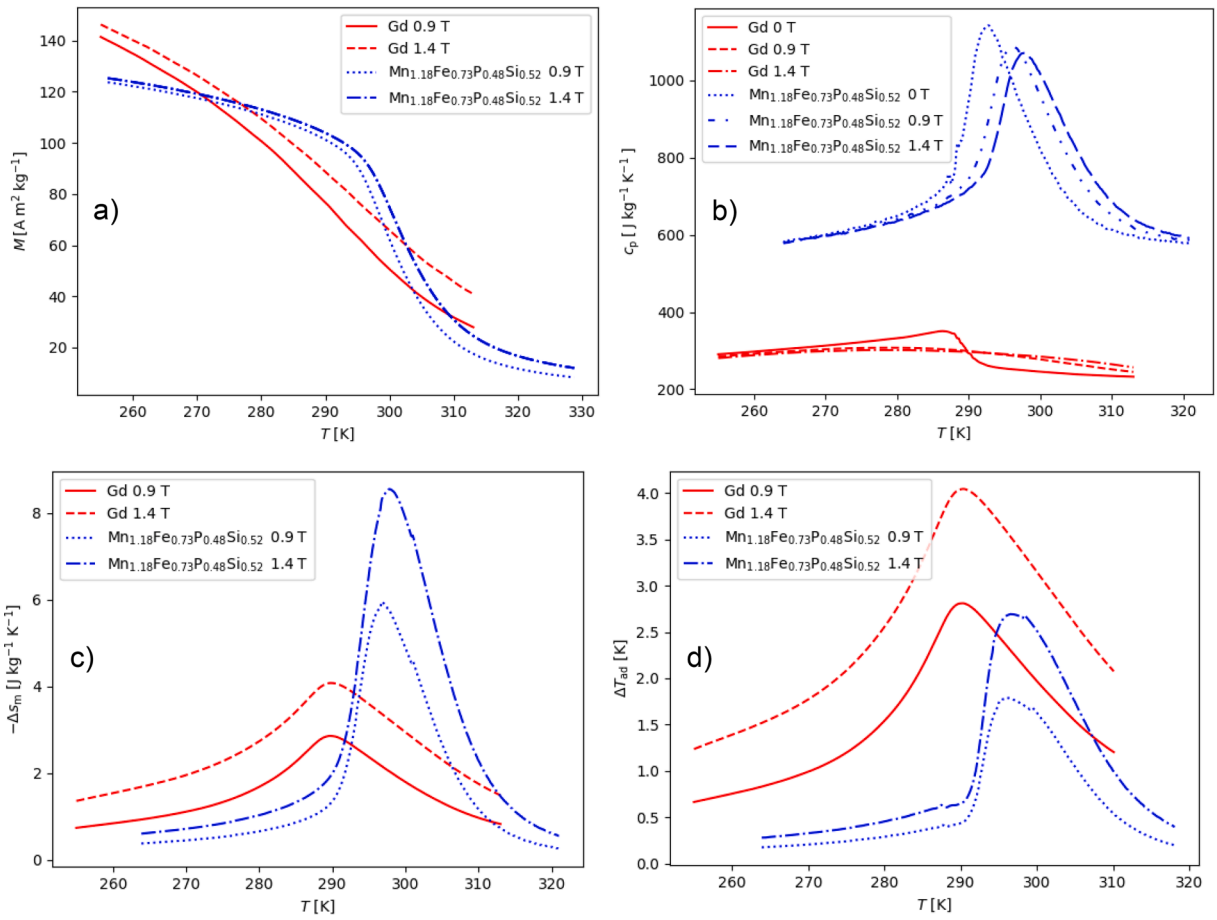

Fig. 3. Magnetization (a), heat capacity (b), magnetic entropy change (c), and adiabatic temperature change (d) of the $Mn_{1.18}Fe_{0.73}P_{0.48}Si_{0.52}$ material as a function of temperature in comparison with the same properties of Gd.

$$COP_{hp} = \frac{\dot{Q}_h}{\dot{W}_{pump} + \dot{W}_m} \tag{11}$$

$$\eta_{Carnot} = \frac{COP_{hp}}{COP_{Carnot}} \tag{12}$$

$$\dot{W}_m = \frac{1}{\tau}\int_0^L \int_0^\tau \rho_s A_{cs}(1-\epsilon)T_s\left(\frac{ds}{dt}\right)dt\,dx \tag{13}$$

2.3. Model inputs

Fig. 1 shows the fluid flow and magnetic field profiles used in the simulations. These profiles resemble the profiles of a rotating-magnet, multi-bed magnetocaloric heat-pump device as the one developed by Huang et al. (2019) [69]. Stagnation periods are possible in this particular device thanks to solenoid valves that allow the reciprocating flow in synchronization with the magnetic field. Vieira et al. (2023) measured the flow profiles that are attained when using commercial solenoid valves and found that the resulting profiles are very close to a trapezoidal shape. They found only small discrepancies in the results obtained when using the measured profiles vs the trapezoidal profiles in a numerical model [70].

The overall regenerator geometry considered for the simulations presented in Fig. 2 also matches with the one proposed by Huang et al. (2019) [69]. This overall shape is constrained by the shape and size of the air gap of the magnet, which for the case of the device considered

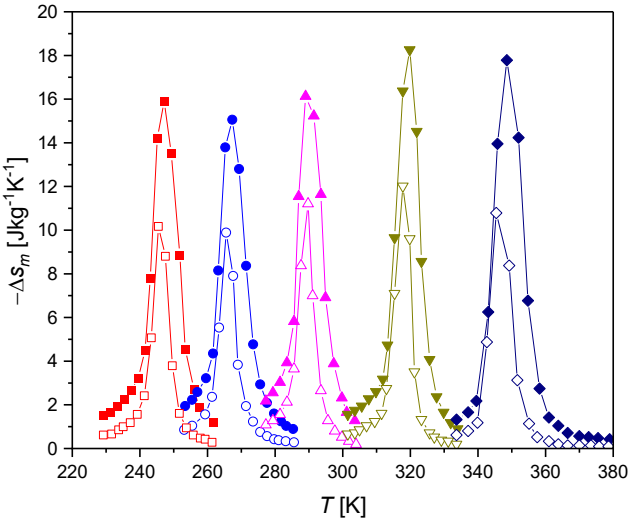

Fig. 4. Magnetic entropy change of $Mn_xFe_{1-x}P_{1-y}Si_y$ for a series of compositions. From left to right x = 1.32, 1.30, 1.28, 1.24, 0.66 and y = 0.48, 0.50, 0.52, 0.54, 0.34. Solid symbols correspond to a magnetic field change from 0 to 2 T and open symbols from 0 to 1 T.
Adapted from [71]

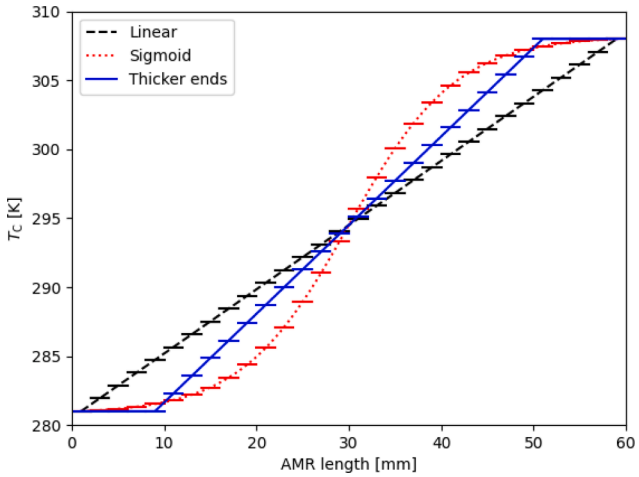

Fig. 5. Curie temperature separation between materials vs the position of each material along the bed for the layering strategies considered in this study: linear distribution of Curie temperatures (dashed line), sigmoid distribution of Curie temperatures (dotted line), and linear distribution with thicker ends (solid line).

here is a C-shaped magnet. Table 3 presents a summary of other key parameters that were used in the simulations. Mass flow rate of HTF corresponds to a single AMR.

2.4. Material properties

Fig. 3 shows some properties of the $Mn_{1.18}Fe_{0.73}P_{0.48}Si_{0.52}$ material, which has been taken as the reference material for this study [52]. This material exhibits a small amount of thermal hysteresis of about 0.6 K, but in Fig. 3 only heating curves are presented. Neglecting thermal hysteresis conducts to an overestimation of AMR performance because smaller MCE is attainable in an MCM with hysteresis. However, the goal of this study is to compare different layering strategies rather than predicting real performance of these AMRs thus including hysteresis will not change the conclusions. Fig. 3 a) shows the isofield magnetization curves for 0.9 T and 1.4 T for this material and for Gd. The sharper transition of the MnFePSi material in comparison with Gd is evident in this figure. Fig. 3 b) shows the specific heat capacity of the MnFePSi material and Gd as a function of temperature for 0 T, 0.9 T and 1.4 T. The first order character of the MnFePSi material is also apparent from this figure. Fig. 3 c) shows the magnetic entropy change, and Fig. 3 d) shows the adiabatic temperature change of the MnFePSi material and Gd for magnetic field changes from 0 T to 0.9 T and from 0 T to 1.4 T. These properties have been calculated from total entropy data. The high specific heat capacity of the MnFePSi compound is responsible for the small adiabatic temperature change that this material exhibits. The properties of the materials in the layered bed were obtained by artificially shifting the properties of the $Mn_{1.18}Fe_{0.73}P_{0.48}Si_{0.52}$ compound to the desired Curie temperatures. Curie temperature is taken in this study as the temperature of the peak of the specific heat of the MCM in zero field. It has been demonstrated that it is possible to continuously tune the Curie temperature of the MnFePSi compound over a wide temperature range by changing the Fe:Mn and the P:Si ratio without compromising the MCE or considerably modifying the thermal hysteresis. This can be seen in Fig. 4 [71]. Therefore, even though artificially created properties are used in this study, it is feasible to produce materials with similar properties in the temperature range used here, from 281 K to 308 K, by using different compositions of the material system MnFePSi.

2.5. Layering strategies

An ideal AMR should have a continuous change in the transition temperature of the material along the bed so that the MCE is maximum at any position [21]. In order to resemble this ideal condition of continuous change in transition temperature, it was decided to compare AMRs of 30 layers. This number of layers is not so large to consider that this AMR has a continuous change in Curie temperature, but it is large enough taking into account the conclusions of numerical simulations with layered AMRs using $La(Fe,Mn,Si)_{13}H_y$ materials which indicated that using more than 15 layers would generally not improve the performance of the AMR [26]. This was also confirmed by prior simulations (not presented here) for the material system MnFePSi that is considered in this study. The question is how to distribute the transition temperatures along the bed so that the temperature at every section of the AMR actually fluctuates around its transition temperature.

Fig. 5 presents a Curie temperature vs AMR length diagram for the three basic layering strategies that are considered in this study. In the three cases, 30 layers of MCM were considered with Curie temperatures ranging from 281 K to 308 K (the design temperature span) each with a length of 2 mm (L_{AMR} / 30). The base layering strategy, which is shown in black dashed line in Fig. 5, is a linear distribution of Curie temperatures along the bed, i.e. an uniform separation of Curie temperatures and layers of equal length. The second layering strategy, shown in red dotted line in Fig. 5, corresponds to a distribution of Curie temperatures that follows a sigmoidal function, i.e. the separation of Curie temperature is smaller between the layers located near the ends of the AMR and bigger for the layers near the middle, with all layers of the same length. The Curie temperature of each layer as a function of the position of its middle point is obtained by using equation (14), where the values of the parameters are approximately: a = 27.37, b = 0.17, c = 30.00, and d =

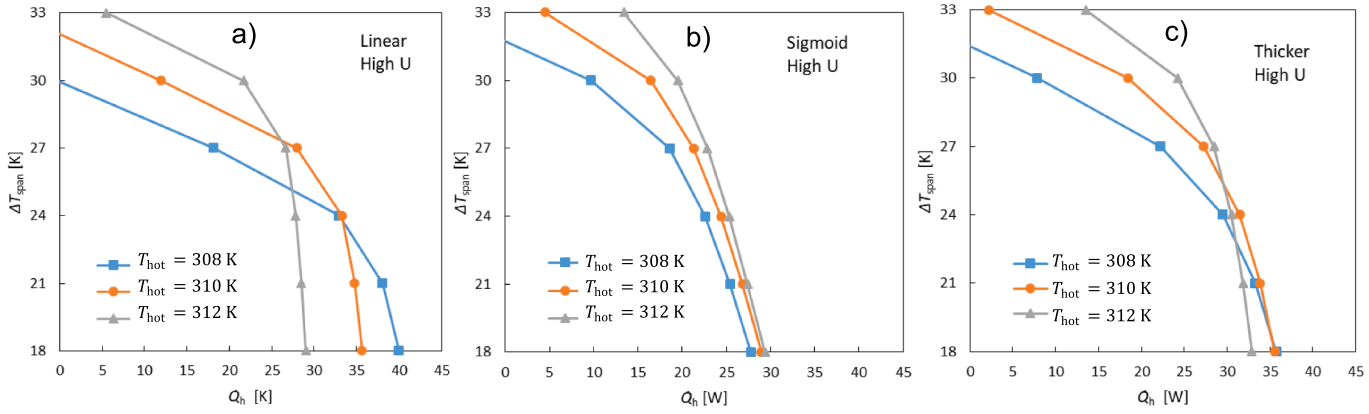

Fig. 6. Temperature span vs heating capacity of an AMR with a linear distribution of Curie temperatures (a), a sigmoid distribution of Curie temperatures (b), and a linear distribution with thicker end layers (c) for a case with large flow rate 37.5 g/s and low frequency 0.75 Hz, i.e. high utilization. Three hot side temperatures are considered T_{hot} = [308, 310, 312] K.

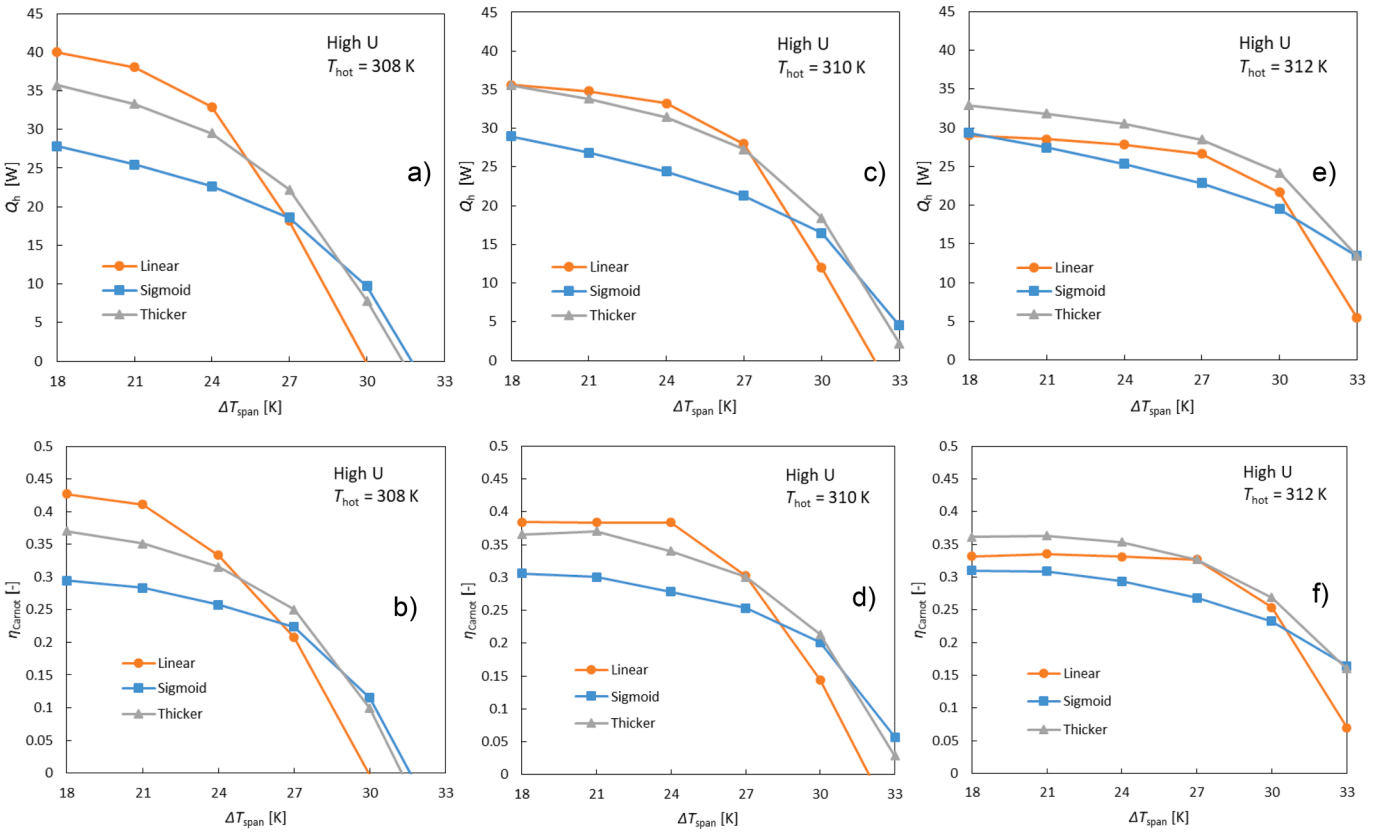

Fig. 7. Heating capacity and second law efficiency vs temperature span of AMRs working under high utilization conditions (max. mass flow rate 37.5 g/s and frequency 0.75 Hz) for T_{hot} = 308 K (a, b), T_{hot} = 310 K (c, d) and T_{hot} = 312 K (e, f) and for the three layering strategies considered.

280.82. The motivation behind considering this shape comes from the fact that the temperature distributions of the solid material observed in numerical simulations of single layer AMRs are flat at the cold end of the AMR during the cold-to-hot blow and flat at the hot end during the hot-to-cold blow (see [57] as an example), which is a consequence of the heat exchange between fluid and solid. Therefore, using a sigmoidal shape for the distribution of Curie temperatures could lead to have each MCM fluctuating around its Curie temperature and thus to maximize the MCE along the bed. In the third layering strategy, shown in blue solid line in Fig. 5, it was considered that five layers at each end have the same Curie temperature and the rest internal layers follow a linear distribution. This is the same as considering that there are 22 layers of MCM in the bed with uniform separation of Curie temperatures, with the length of the first and the last layers being 10 mm each (L_{AMR} / 6), and the length of the middle layers being 2 mm each (L_{AMR} / 30). An analysis about the influence of the length of these thicker layers is presented in section 3.4.

$$T_C = \frac{a}{1 + e^{-b\ (x-c)}} + d \tag{14}$$

3. Results and discussion

All heating capacities presented in this section correspond to a single AMR. Two scenarios were considered in terms of combination of operating conditions. First, the results of a high utilization scenario, i.e. large mass flow rate (37.5 g/s) and low frequency (0.75 Hz), will be presented. Then, the results of a low utilization scenario, i.e. smaller mass flow rate (25.0 g/s) and higher frequency (4.5 Hz), will follow. These two combinations of flow rates and frequencies correspond to the following utilization values: U_{high} = 0.53 and U_{low} = 0.06, which were calculated using equation (15).

$$U = \frac{c_f \int_{t_1}^{t_2} \dot{m}_f dt}{A_{cs} L_{AMR} (1 - \epsilon) \rho_s c_s} \tag{15}$$

Where c_s = 800 $Jkg^{-1}K^{-1}$ was taken as reference heat capacity of the MCM and corresponds approximately to the half peak heat capacity, ρ_s = 6100 $kg\,m^{-3}$, c_f = 4200 $Jkg^{-1}K^{-1}$, and t_1 and t_2 correspond to the beginning and end of the cold-to-hot blow process.

3.1. High utilization scenario

Fig. 6 a), b), and c) show the temperature span vs heating capacity curves for the three layering strategies at three different hot side temperatures. Fig. 7 a), c), and e) show the same information presented in Fig. 6 in a different way to facilitate the comparison of the performance between the different layering strategies.

As can be seen in Fig. 6, the AMR with a sigmoidal distribution of Curie temperatures is less sensitive to the changes in the hot and cold temperatures compared to the other two. For example, for a temperature span of 18 K, the heating capacity of the AMR in Fig. 6 a) changes from 29.0 W to 40.0 W when the hot side temperature changes from 312 K to 308 K, corresponding to a variation of 37.9 %, whereas this variation would be 5.6 % in Fig. 6 b) and 8.7 % in Fig. 6 c). An AMR that is less sensitive to changes in the hot and cold temperatures is desirable in magnetocaloric heat pumps, which can be continuously subjected to changes in the temperatures of the heat source and heat sink during operation, even though the temperature span of the AMR can also be fixed by using a control system. Comparing the AMR with sigmoid distribution of Curie temperatures and the one with linear distribution of Curie temperatures but thicker end layers, the latter produces greater heating capacities for almost all combinations of T_{hot} and ΔT_{span} that were simulated, although it exhibits more variation in heating capacity with changes of the hot side temperature.

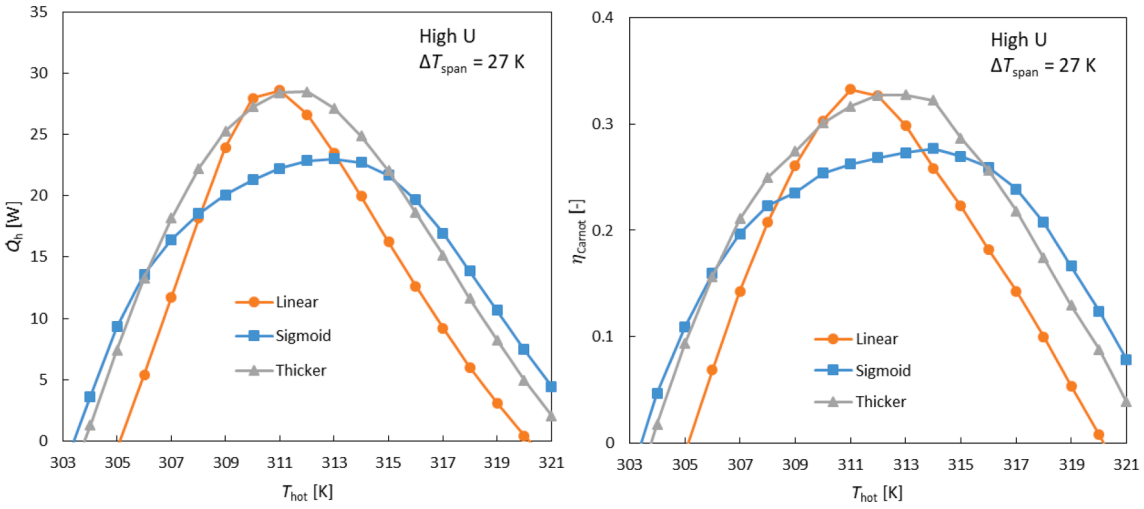

Fig. 8. Heating capacity (left) and second law efficiency (right) as a function of hot side temperature for a fixed temperature span of 27 K for the high utilization scenario.

In Fig. 7 we compile the performance of the three AMRs in the high utilization scenario. Fig. 7 a), c), and e) show heating capacities vs temperature span curves while figures b), d), and f) show the second law efficiency as a function of temperature span. Second law efficiency was calculated with equation (12). The AMR with linear distribution of Curie temperatures performs better than the other two in terms of heating capacity and second law efficiency when the hot side temperature is below 310 K and the temperature span is smaller than 27 K. The AMR with linear distribution of Curie temperatures and thicker ends performs better than the other two when the hot side temperature is 312 K. This suggests that the optimum hot side temperature is not the same for the three AMRs even though the Curie temperatures of the MCMs range between 281 K and 308 K in all three cases.

An additional observation in Fig. 7 is that the AMR with a sigmoid distribution of Curie temperatures produces a greater heating capacity and higher second law efficiency than the other two for temperature spans above 30 K. However, for such large temperature spans the heating capacity reduces considerably, and thus it is not expected that an AMR operates under such conditions. It is also remarkable from Fig. 7 that the AMRs with linear distribution of Curie temperatures and the one with thicker ends exhibit bigger changes in their second law efficiency at $\Delta T_{span} = 27$ K (from approx. 20 % and 25 % respectively to approx. 33 % in both cases) when T_{hot} changes from 308 K to 312 K compared with the AMR with a sigmoid distribution of Curie temperatures (from approx. 22 % to approx. 26 %). This is also an indication of the lower sensitivity to changes of operating temperatures that the sigmoid AMR has. Furthermore, none of the three simulated AMRs produces second law efficiencies over 40 % for a $\Delta T_{span} = 25$ K while a vapour compression heat pump can achieve second law efficiencies of the order of 43 % for the same ΔT_{span} according to Kiss & Infante Ferreira (2016) [72]. Finally, by looking at overall trends in Fig. 7 a), c), and e), it is possible to say that greater heating capacities for small temperature spans are attainable when $T_{hot} = 308$ K, and larger zero-load temperature spans when $T_{hot} = 312$ K. This is because a better alignment of the range of Curie temperatures of the MCMs with the range of operating temperatures is only possible by decreasing T_{hot} for small temperature spans or increasing T_{hot} for large temperature spans.

In order to confirm that the optimum hot side temperature is not the same for the three AMRs, additional simulations were carried out to see the influence of the hot side temperature for a fixed temperature span of 27 K (the design ΔT_{span}). Fig. 8 shows the results of these additional simulations for the high utilization scenario. The optimum hot side temperature is equal to 311 K for the AMR with a linear distribution of Curie temperatures, 313 K for the one with a distribution of Curie temperatures following a sigmoid function, and 312 K for the AMR with the linear distribution and thicker ends. This must be considered in the design process of a layered AMR. For example, if the design point of an AMR corresponds to $T_{hot} = 308$ K, $T_{cold} = 281$ K, and the above-mentioned flow rate and frequency and a linear distribution of Curie temperatures with thicker end layers is chosen, the Curie temperatures of the materials should range between approximately 277 K and 304 K (instead of 281 K and 308 K as it was simulated here) so that the maximum performance is obtained when $T_{hot} = 308$ K. Fig. 8 shows that the AMR with thicker ends performs better in terms of heating capacities and second law efficiencies in comparison with the one using a linear distribution of Curie temperatures when the hot side temperature (and the cold side temperature since $\Delta T_{span} = 27$ K is fixed in this figure) moves away from the optimum. In other words, as mentioned above, when using thicker ends the AMR becomes less sensitive to changes in the operating temperatures. It is relevant to remark that for ΔT_{span} larger than 27 K the hot side temperature that produces the maximum heating power is higher than the one shown in Fig. 8 and vice versa, because only by increasing (or decreasing) T_{hot} the working temperature range of the AMR, i.e. $[T_{cold}, T_{hot}]$, can be better aligned with the range of Curie temperatures of the materials to maintain all layers as active and the MCE as large as possible. This can also be seen in Fig. 6 for the 3 layering strategies considered.

Fig. 9 a), c), and e) show the total entropy vs temperature curves at 0 T and 1.4 T for the first MCM adjacent to the cold side of the AMR, MCM number 16 near the middle of the AMR, and the MCM adjacent to the hot side. The curves corresponding to the other MCMs are not shown to avoid excessive overlapping. A different reference point has been chosen for the total entropy of each layer in order to see the peak MCE happening in the same total entropy range although in the own temperature range of each MCM. The horizontal lines in these three figures enclose the region of each material where the $\Delta T_{ad} \geq 2$K, an explanation of which can be found in the appendix. The thermodynamic cycles experienced by the first, the middle, and the last nodes in the discretized solid domain is depicted in red (for the colour references the reader is referred to the online version of this article) whereas the light blue region corresponds to the region where the thermodynamic cycles of the rest of the nodes in the discretized solid domain occur. The performance data used for constructing these diagrams correspond to those of the points of maximum heating capacity of Fig. 8. These diagrams are useful to visualize how well the MCMs are aligned in their full thermodynamic cycle with the temperature range of maximum MCE. In Fig. 9 a) and e), corresponding to the AMRs with linear distribution of Curie temperatures and linear distribution with thicker ends respectively, most of the

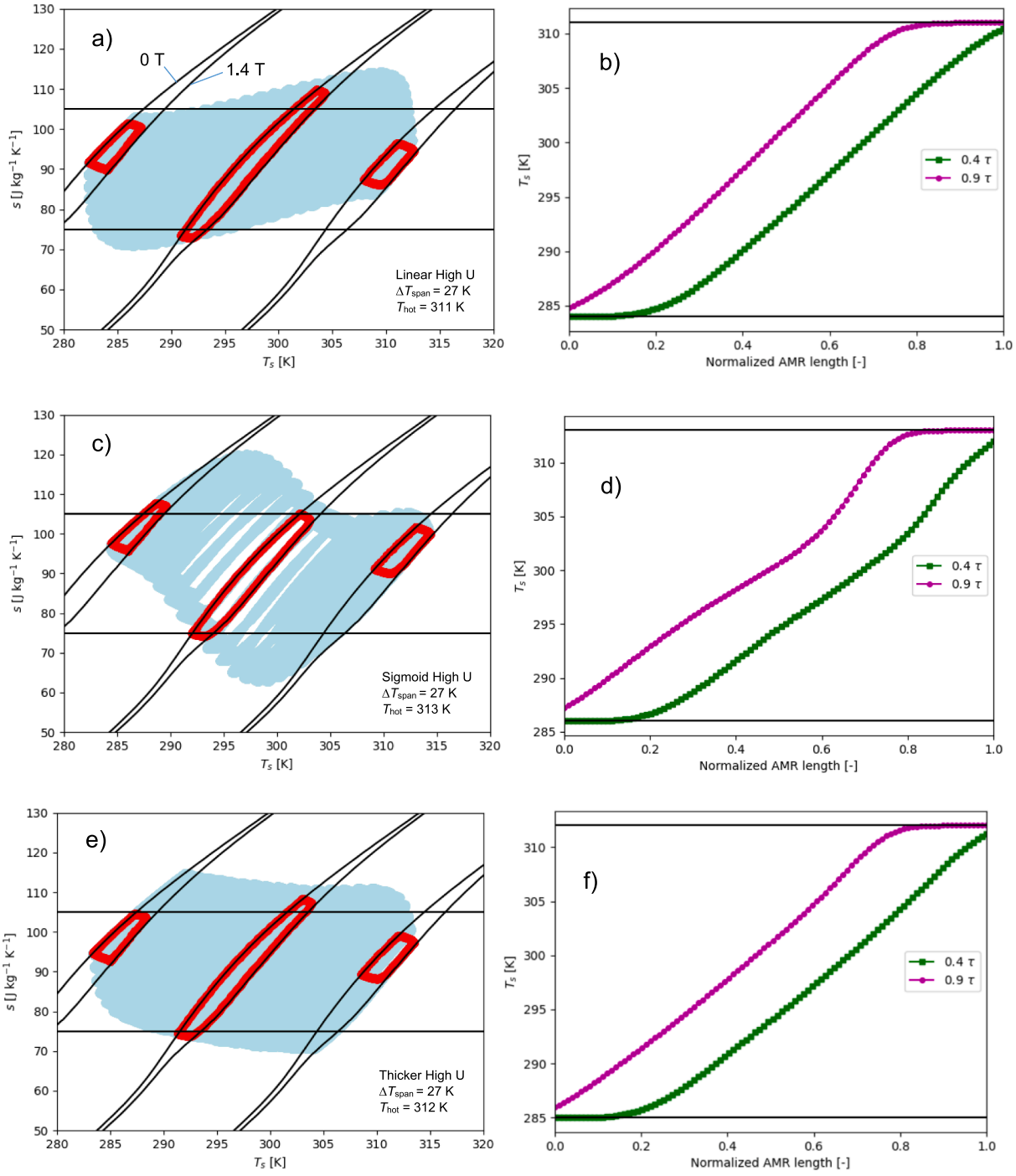

Fig. 9. (left) Thermodynamic cycles in a total entropy vs temperature diagram and (right) temperature distributions of the solid material at $t = 0.4\tau$ (near the end of cold-to-hot blow: green squares) and $t = 0.9\tau$ (near the end of hot-to-cold blow: magenta circles). (a) and (b) correspond to the AMR with linear distribution of Curie temperatures, (c) and (d) correspond to the AMR with a distribution of Curie temperatures following a sigmoid shape, and (e) and (f) correspond to an AMR with linear distribution of Curie temperatures and thicker ends. Region between horizontal lines in (a), (c) and (e) correspond to an $\Delta T_{ad} \geq 2$K for each material. Horizontal lines in (b), (d) and (f) represent T_{cold} and T_{hot} for each case.

MCMs experience thermodynamic cycles that are well aligned with the region of maximum MCE of each MCM. On the contrary, in Fig. 9 c), corresponding to the AMR with a sigmoid distribution of Curie temperatures, the materials close to the cold side experience thermodynamic cycles in which the magnetization process is out of the range of maximum MCE. For this reason, poorer cooling and heating capacities are attainable. On the other hand, Fig. 9 b), d), and f) show the temperature distributions of the solid material near the end of the cold and hot blow processes respectively. These figures suggest that the layering strategy influences the shape of the temperature distribution profiles with the linear layering strategies also producing more linear temperature distributions in the middle part of the AMR when the operating temperature span is close to the design temperature span.

3.2. Low utilization scenario

In the low utilization scenario, see Fig. 10, the three AMRs produce slightly poorer heating capacities for temperature spans equal or below

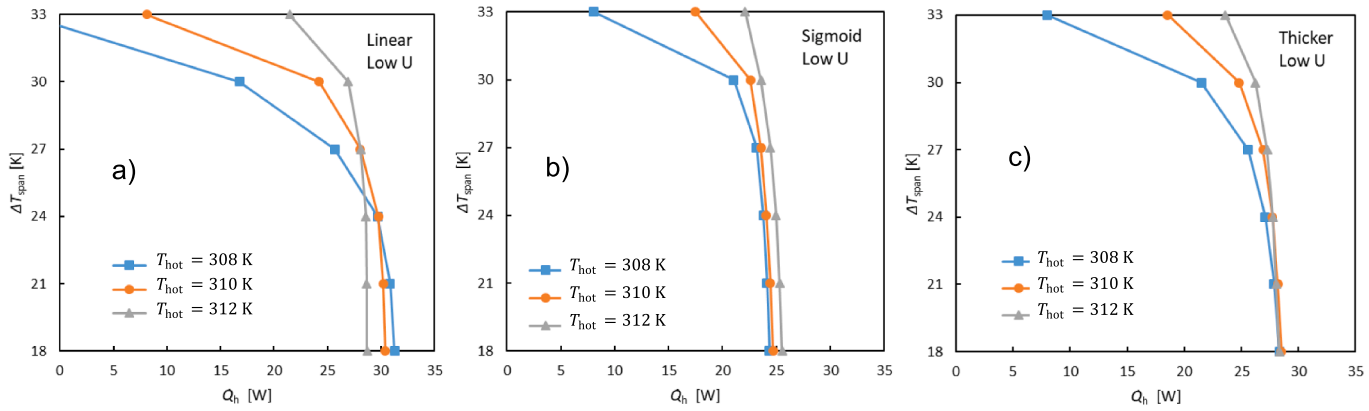

Fig. 10. Temperature span vs heating capacity of an AMR with a linear distribution of Curie temperatures (a), a sigmoid distribution of Curie temperatures (b), and a linear distribution with thicker end layers (c) for a case with small flow rate 25 g/s and high frequency 4.5 Hz, i.e. low utilization.

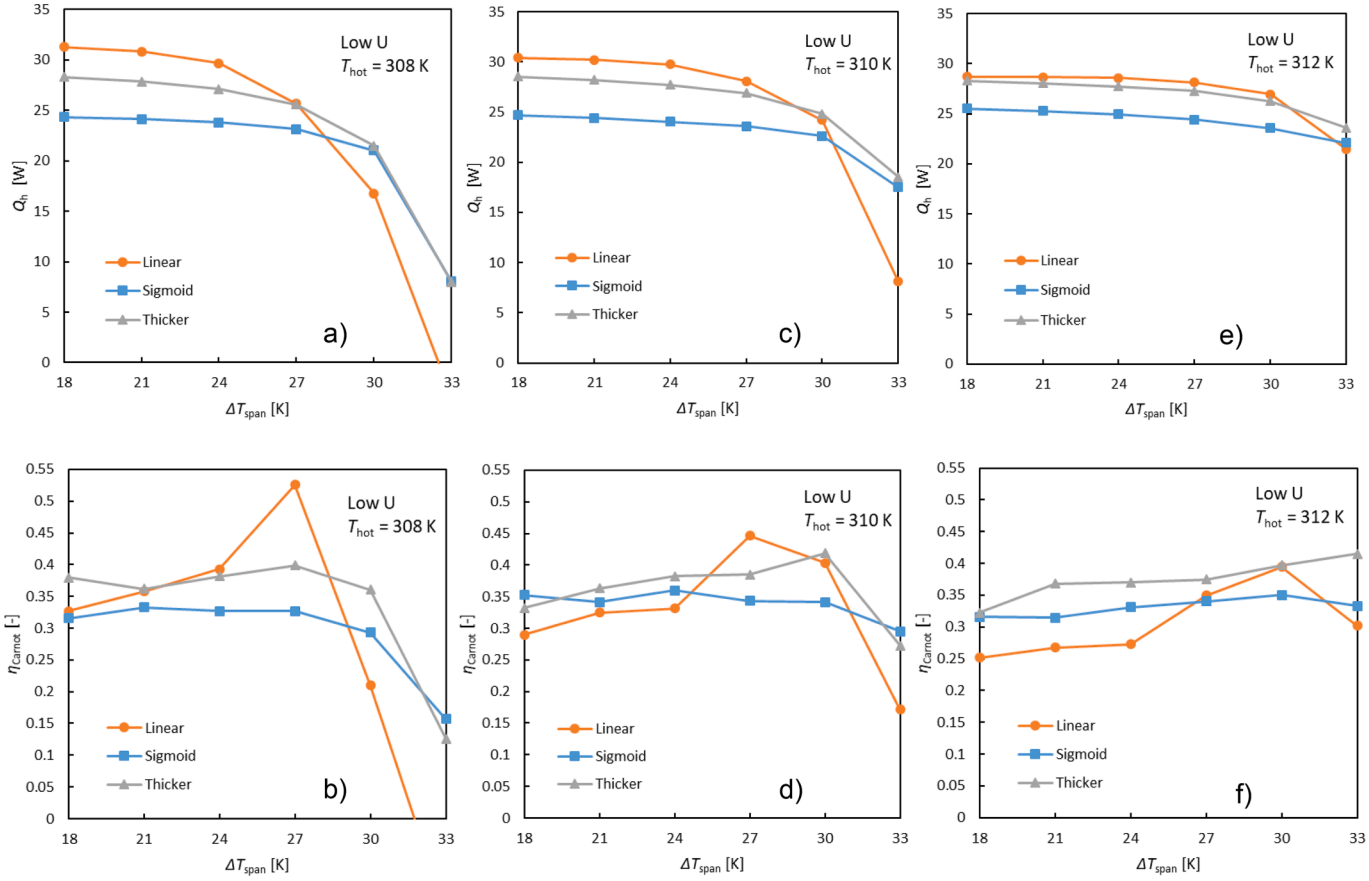

Fig. 11. Heating capacity and second law efficiency vs temperature span of AMRs working under low utilization conditions (max. mass flow rate 25 g/s and frequency 4.5 Hz) for T_{hot} = 308 K (a, b), T_{hot} = 310 K (c, d) and T_{hot} = 312 K (e, f) and for the three layering strategies considered.

27 K and also larger zero-load temperature spans in comparison with the high utilization scenario, see Fig. 6. It is also evident when comparing Fig. 6 and Fig. 10 that the three AMRs become more sensitive to changes in the hot side and cold side temperatures in the high utilization scenario. Regarding Fig. 10, in a low utilization scenario, the three AMRs perform similarly although the one with the linear distribution of Curie temperatures is again slightly more sensitive to changes of the hot side and cold side temperatures.

Fig. 11 shows the heating capacity and second law efficiency of the three different AMRs comparatively for the low utilization scenario. Fig. 11 a) and b) correspond to a hot side temperature of 308 K, c) and d) to 310 K, and e) and f) to 312 K. For the low utilization scenario, the AMR with a linear distribution of Curie temperatures and thicker ends performs better in terms of second law efficiency for a wide variety of operating temperatures. However, the AMR with a linear distribution of Curie temperatures performs better in terms of heating capacity for temperature spans below 27 K for the three hot side temperatures considered.

Regarding the efficiencies shown in Fig. 11, it can be seen that the peaks move to larger ΔT_{span} when T_{hot} increases. This can be due to a better alignment of the Curie temperature of the MCMs in the AMRs with the working temperatures. It is also noticeable in Fig. 10 and Fig. 11 that

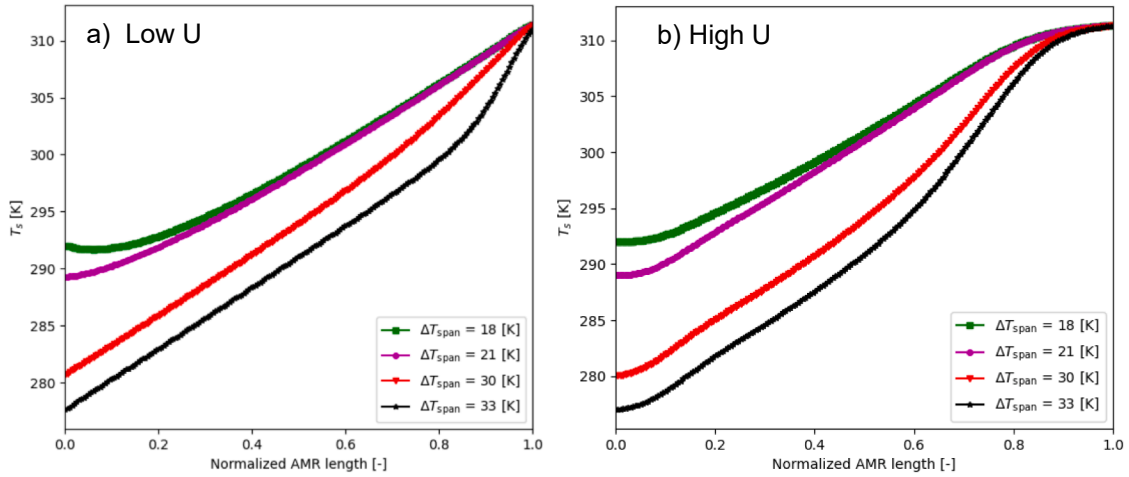

Fig. 12. Solid temperature distribution at ¼ of the cycle period for the AMR with linear distribution of Curie temperatures in the low utilization scenario (a) and high utilization scenario (b), and $T_{hot} = 310$ K.

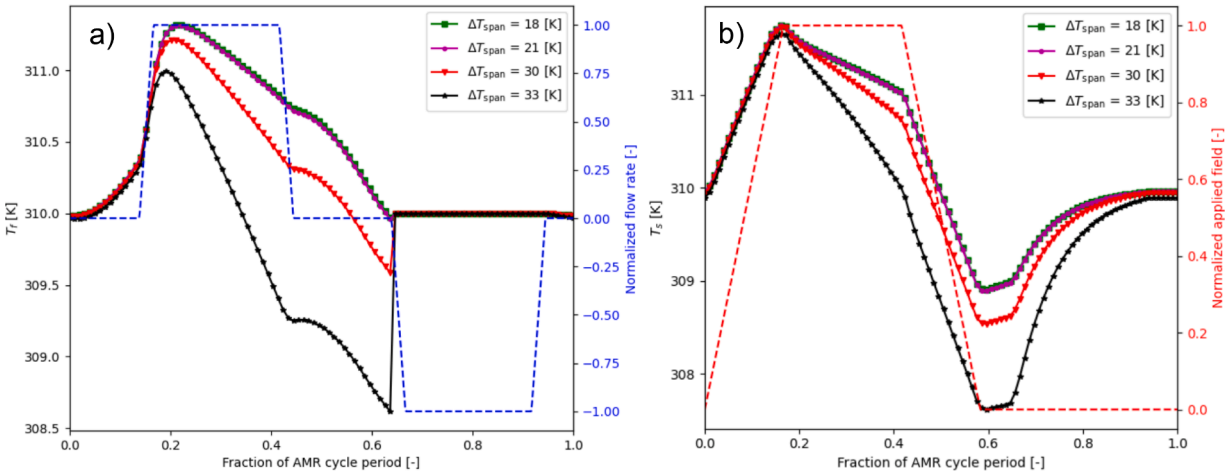

Fig. 13. Temperature of fluid (a) and solid (b) at $x = L$ (hot side of the AMR) as a function of time for 4 different temperature spans. An AMR that follows a linear distribution of Curie temperatures in a low utilization scenario is considered in this figure, and $T_{hot} = 310$ K. Fluid flow and magnetic field profiles are also depicted using dashed lines to facilitate visualization of the different stages of the AMR cycle.

for temperature spans below 24 K these AMRs produce essentially the same heating capacity. A similar behaviour was observed by Jacobs and co-workers (2013), who tested a magnetocaloric refrigerator prototype equipped with 12 multi-layer AMR beds of LaFeSiH compounds [14]. Smith et al. also showed a figure that suggest that graded AMRs typically exhibit an almost constant cooling capacity for small to medium temperature spans before dropping to zero after a critical point [17]. This occurs because the temperature of the portion of the AMR closest to the hot end, which is the section of the AMR responsible for producing the heating capacity, fluctuates around the same values for temperature spans that are smaller than the design temperature span when the hot side temperature is fixed. This condition is easier to achieve in low utilization conditions, but it is also observable in some cases under high utilization conditions. Fig. 12 a) shows the solid temperature distribution at $t = 0.25\tau$ for the AMR with linear distribution of Curie temperatures when $T_{hot} = 310$ K and $\Delta T_{span} = [18, 21, 30, 33]$ K under low utilization conditions. Fig. 12 b) shows the same for the high utilization conditions. It can be seen that the temperature of the solid (and also the temperature of the fluid even though not depicted in this figures) for temperature spans equal to 21 K and 18 K is nearly the same from roughly 50 % of the AMR length to the hot end in the low utilization condition. In the high utilization condition, a smaller portion of the AMR exhibit nearly the same temperatures for temperature spans equal to 18 K and 21 K. The heating capacities in the low utilization scenario are 30.4 W and 30.2 W for temperature spans 18 K and 21 K respectively, whereas in the high utilization scenario the heating capacities are 35.6 W and 34.8 W for temperature spans 18 K and 21 K respectively. Fig. 13 also confirms that for the points with approximately equal heating capacity and different temperature spans of Fig. 10 the temperature of fluid and solid at the hot end of the AMR coincide.

In Fig. 12 a), the temperature distribution of the solid corresponding to a temperature span of 18 K has a minimum at a normalized AMR length of approximately 0.1. A similar behaviour has been observed in experiments with two-layer AMRs conducted by Teyber et al. (2016) [36]. They attribute this behaviour to heat transfer from the AMR to ambient through the casing because ambient temperature was smaller than T_{cold} in such experiments. Ambient temperature was fixed at 288 K in our simulations while T_{cold} is 292 K for the case under consideration. So, heat leaks to ambient could explain that the lowest temperature is not located at the cold end of the AMR when T_{cold} is above ambient temperature.

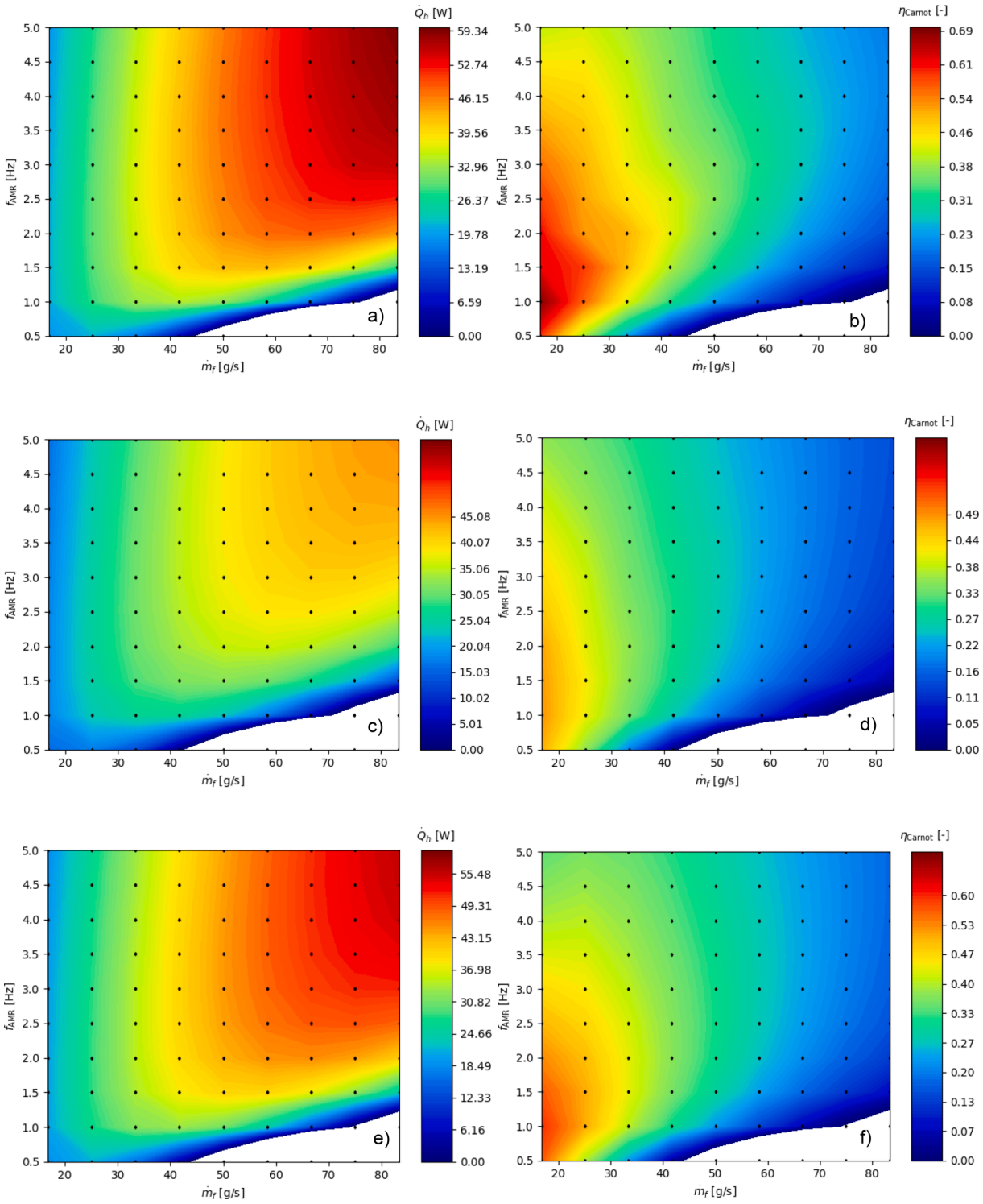

Fig. 14. Heating capacities in [W] (left) and second law efficiencies (right) of the three selected layering strategies, linear (a), (b), sigmoid (c), (d), and linear with thicker ends (e), (f) as a function of cycle frequency and mass flow rate for $T_{hot} = 310$ K and $\Delta T_{span} = 27$ K.

3.3. Performance for other ranges of operating conditions

Given that the results presented above are only for two utilization values, a bigger range of operating conditions in terms of flow rate and AMR cycle frequency was explored to see if there is an operating point (or region) for which the AMR that follows a sigmoidal distribution of Curie temperatures achieves a better matching between temperature distribution and the region of maximum MCE of each material in order to produce greater heating capacities than the other two. Fig. 14 shows the results of this group of simulations for which $T_{hot} = 310$ K, $\Delta T_{span} = 27$ K, the mass flow rate ranged between 16.66 and 83.33 g/s and the cycle frequency between 0.5 and 5 Hz.

As it can be seen in Fig. 14, the AMR with the linear distribution of Curie temperatures produces the greatest maximum heating capacity of the three AMRs. These results follow the same trend as in Fig. 7 c) and Fig. 11 c) where the AMR with linear distribution of Curie temperatures outperforms the other two when $T_{hot} = 310$ K and $\Delta T_{span} = 27$ K. A real maximum heating capacity is not observable in the simulated range for

any of the three AMRs, but larger flow rates and frequencies are difficult to achieve in practice because of the reciprocating nature of the flow and because of significant increases in pressure gradient. For the point of largest flow rate and frequency considered in this group of simulations the maximum calculated pressure gradient was approximately 3.2 bar. This pressure gradient could be reduced by optimizing the shape of fluid channels [73,74]. On the other hand, second law efficiency is also depicted in Fig. 14 for the three AMRs. For the particular combination of operating temperatures, the AMR with the linear distribution of Curie temperatures also produces higher second law efficiencies reaching a maximum of 69 % while the maximum is 49 % for the sigmoidal and 60 % for the one with thicker ends. This difference in performance is mainly due to greater heating capacities of the linear case given that the magnetic power input and pumping power are comparable for the three cases. The pumping power of the three AMRs at the maximum efficiency point is approximately the same given that the maximum occurs at the same flow rate and frequency for the three cases.

3.4. Influence of end layer thickness

Fig. 15 presents the results of an additional group of simulations carried out to see the influence of the thickness of the end layers on the performance of an AMR with linear distribution of Curie temperatures and thicker end layers. These simulations were carried out for a $\Delta T_{span} = 27$ K, with $T_{cold} = 285$ K and $T_{hot} = 312$ K, which was the optimum working temperature range found in Fig. 8. The flow rate was fixed equal to 37.5 g/s, and three frequencies were considered in order to produce three different utilizations, 0.75 Hz, 1.5 Hz, and 2.25 Hz. The same 22 MCMs introduced in section 2.5 for the third layering strategy (thicker end layers) are also used here, the Curie temperatures of which range between 281 K and 308 K. The total length of the AMR, L_{AMR}, was fixed equal to 60 mm for all cases as in the previous sections, and the length of the inner layers was defined as $L_{inner} = (L_{AMR} - 2\,L_{end})/20$. It was found that the optimum end layer thickness for a fixed total AMR length depends on the utilization (or penetration of fluid in the AMR). The higher the utilization (and penetration of fluid) the greater the length of the end layer that maximizes the heating capacity. This can be seen in Fig. 15, where for lower frequencies, i.e. longer cycle periods and thus longer blow time and larger penetration distances, the maximum heating capacity moves to greater end layer thicknesses. By fitting the data points to 4th order polynomials, the maxima were found at end layer thicknesses equal to 5.63 mm, 7.11 mm, and 8.57 mm for frequencies 2.25 Hz, 1.50 Hz, and 0.75 Hz respectively.

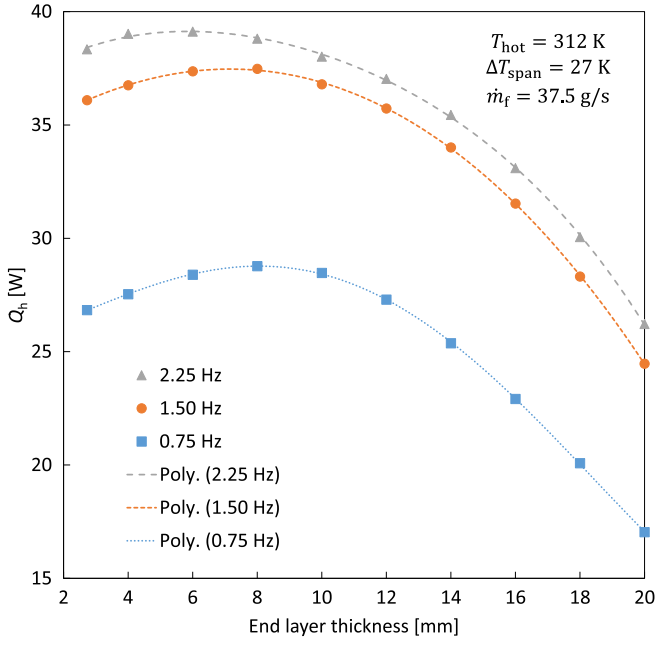

Fig. 15. Influence of the end layer thickness on the heating capacity of a 22-layer AMR for a fixed $\Delta T_{span} = 27$ K. Lines correspond to 4th order polynomial fits.

4. Conclusions

A one-dimensional numerical model was used to study the performance of layered AMRs composed of materials of the MnFePSi family arranged in three different layering strategies: one following a linear distribution of Curie temperature, a second with a distribution of Curie temperatures that follows a sigmoid function, and a third one in which there is a linear distribution of Curie temperatures with thicker end layers. The following can be concluded from this study:

- It was found that a layered AMR with a linear distribution of Curie temperatures whose end layers are thicker than the middle ones can perform better in terms of heating capacity for a wide range of operating temperatures in a high utilization scenario when compared to an AMR with linear distribution of Curie temperatures and uniform layer length. This AMR is also less sensitive to changes in the hot and cold reservoir temperatures, which is advantageous given that these parameters usually fluctuate during the operation of a heat pump.
- It was also found that the optimum hot side temperature depends on the selected layering strategy (besides depending also on the operating conditions flow rate and frequency). Even though the Curie temperatures of the materials, which in this study are defined as the temperatures of the peaks of the heat capacity in zero field, range from 281 K to 308 K in all three cases, the optimum performance with temperature span 27 K, flow rate 37.5 g/s, and a frequency of 0.75 Hz is observed when the hot side temperature is 311 K, 313 K and 312 K for the AMRs with linear distribution of Curie temperatures, sigmoid distribution, and linear distribution with thicker ends respectively.
- The selected layering strategy has an influence on the shape of the temperature distributions. A linear distribution of Curie temperatures also produces a more linear solid temperature distribution in the middle part of the AMR in comparison with the distribution of Curie temperatures that follows a sigmoid function. This applies when the operating temperature span is close to the design temperature span.
- The AMR with a linear distribution of Curie temperatures and uniform layer length outperforms the other two in terms of maximum heating capacity and second law efficiency when a wider range of flow rates and frequencies was explored for a fixed hot side temperature of 310 K and temperature span of 27 K. The heating capacity of this AMR reaches a maximum equal to approximately 59.3 W for a frequency of 5 Hz and a mass flow rate of 83.3 g/s while for the same operating conditions the AMR with a sigmoidal distribution of Curie temperatures reaches 45.1 W and the one with thicker end layers 55.5 W. The maximum second law efficiency is 69 % for the AMR with a linear distribution of Curie temperatures, and 49 % and 60 % for the AMRs with sigmoidal distribution and thicker end layers respectively. The maximum second law efficiency occurs when the mass flow rate is 16.6 g/s and frequency is 1 Hz in all three cases.
- In AMRs with thicker end layers, it was found that for a given set of operating conditions (flow rate, frequency, T_{hot}, and T_{cold}) there is an optimum length of the end layers that maximizes the heating capacity. This length tends to increase as the utilization increases.

Declaration of Competing Interest

The authors declare that they have no known competing financial interests or personal relationships that could have appeared to influence the work reported in this paper.

Data availability

Data will be made available on request.

Acknowledgment

This project is implemented with support from the MMIP 3&4 scheme of the Ministry of Economic Affairs & Climate Change and the Ministry of the Interior & Kingdom Relations of the Netherlands. Diego Pineda Quijano thanks Bowei Huang for the fruitful discussions.

Appendix A

In this section some details about the construction of the S-T diagrams of Fig. 9 are presented. Fig. 16 a) shows the adiabatic temperature change of the base material $Mn_{1.18}Fe_{0.73}P_{0.48}Si_{0.52}$ as a function of temperature for a magnetic field change from 0 to 1.4 T. Fig. 16 b) shows the total entropy of the same material as a function of temperature for two magnetic fields, 0 T and 1.4 T. The vertical lines in Fig. 16 a) enclose the temperature range where the adiabatic temperature change is larger than 2 K. This temperature range is also drawn as vertical lines in Fig. 16 b). The entropy values of the points where these vertical lines intersect the zero field entropy curve correspond approximately to 75 and 105 $Jkg^{-1}K^{-1}$. The same applies for the other materials in the bed but in their own temperature range.

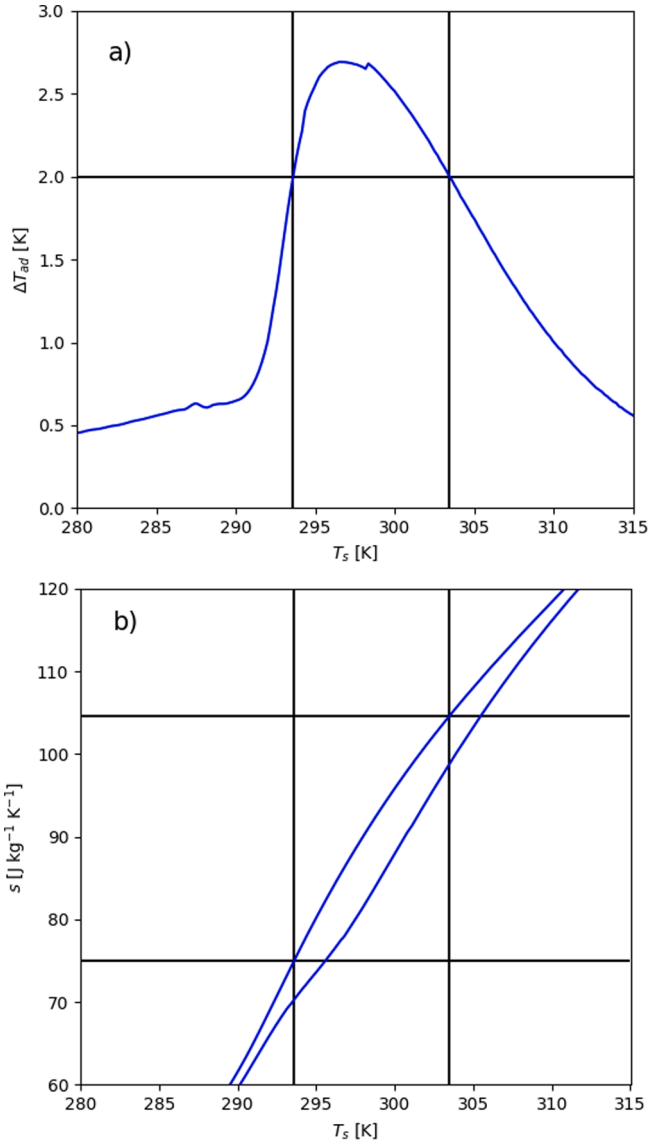

Fig. 16. Adiabatic temperature change vs temperature (a), and total entropy vs temperature (b) of the material $Mn_{1.18}Fe_{0.73}P_{0.48}Si_{0.52}$. Vertical lines on figure (a) enclose the temperature range where the adiabatic temperature change is larger than 2 K.

References

[1] H. Lv, H. Ma, N. Mao, T. He, Boiling heat transfer mechanism of environmental-friendly refrigerants: A review, Int. J. Refrig. 133 (2022) 140–7007, https://doi.org/10.1016/j.ijrefrig.2021.10.007.
[2] W. Goetzler, R. Zogg, J. Young, C. Johnson, Energy savings potential and RD&D opportunities for non-vapor-compression HVAC technologies, 2014. https://doi.org/https://doi.org/10.2172/1220817.
[3] S. Lionte, M. Risser, C. Muller, A 15kW magnetocaloric proof-of-concept unit: Initial development and first experimental results, Int. J. Refrig. 122 (2021) 256–265, https://doi.org/10.1016/J.IJREFRIG.2020.09.019.
[4] S. Dall'Olio, M. Masche, J. Liang, A.R. Insinga, D. Eriksen, R. Bjørk, K.K. Nielsen, A. Barcza, H.A. Vieyra, N. V. Beek, H.N. Bez, K. Engelbrecht, C.R.H. Bahl, Novel design of a high efficiency multi-bed active magnetic regenerator heat pump, Int. J. Refrig. 132 (2021) 243–254. https://doi.org/10.1016/j.ijrefrig.2021.09.007.
[5] None, EU F-gas regulation handbook: keeping ahead of the curve as Europe phases down HFCs, 2015. https://eia-international.org/wp-content/uploads/EIA-F-Gas-Regulation-Handbook.pdf.
[6] A. Kitanovski, J. Tušek, U. Tomc, U. Plaznik, M. Ožbolt, A. Poredoš, Magnetocaloric energy conversion - From theory to applications, 2015.
[7] P.V. Trevizoli, T.V. Christiaanse, P. Govindappa, I. Niknia, R. Teyber, J.R. Barbosa, A. Rowe, Magnetic heat pumps: An overview of design principles and challenges, Sci. Technol. Built Environ. 22 (2016) 507–519, https://doi.org/10.1080/23744731.2016.1171632.
[8] J. Romero Gómez, R. Ferreiro Garcia, A. De Miguel Catoira, M. Romero Gómez, Magnetocaloric effect: A review of the thermodynamic cycles in magnetic refrigeration, Renew, Sustain. Energy Rev. 17 (2013) 74–82, https://doi.org/10.1016/j.rser.2012.09.027.
[9] K.A. Gschneidner, V.K. Pecharsky, Thirty years of near room temperature magnetic cooling: Where we are today and future prospects, Int. J. Refrig. 31 (2008) 945–961, https://doi.org/10.1016/j.ijrefrig.2008.01.004.
[10] D.S. Arnold, A. Tura, A. Ruebsaat-Trott, A. Rowe, Design improvements of a permanent magnet active magnetic refrigerator, Int. J. Refrig. 37 (2014) 99–105, https://doi.org/10.1016/j.ijrefrig.2013.09.024.
[11] L. Griffith, A. Czernuszewicz, J. Slaughter, V. Pecharsky, CaloriSMART: Small-scale test-stand for rapid evaluation of active magnetic regenerator performance, Energy Convers. Manag. 199 (2019), 111948, https://doi.org/10.1016/j.enconman.2019.111948.
[12] P.V. Trevizoli, A.T. Nakashima, J.R. Barbosa, Performance evaluation of an active magnetic regenerator for cooling applications – part II: Mathematical modeling and thermal losses, Int. J. Refrig. 72 (2016) 206–217, https://doi.org/10.1016/j.ijrefrig.2016.07.010.
[13] R. Bjørk, A. Smith, C.R.H. Bahl, N. Pryds, Determining the minimum mass and cost of a magnetic refrigerator, Int. J. Refrig. 34 (2011) 1805–1816, https://doi.org/10.1016/j.ijrefrig.2011.05.021.
[14] S. Jacobs, J. Auringer, A. Boeder, J. Chell, L. Komorowski, J. Leonard, S. Russek, C. Zimm, The performance of a large-scale rotary magnetic refrigerator, Int. J. Refrig. 37 (2013) 84–91, https://doi.org/10.1016/j.ijrefrig.2013.09.025.
[15] A.T.D. Nakashima, F.P. Fortkamp, N.M. De Sá, V.M.A. Santos, G. Hoffmann, G. F. Peixer, S.L. Dutra, M.C. Ribeiro, J.A. Lozano, J.R.B. Jr, A magnetic wine cooler prototype, Int. J. Refrig. 122 (2021) 110–121, https://doi.org/10.1016/j.ijrefrig.2020.11.015.
[16] C. Zimm, A. Boeder, B. Mueller, K. Rule, S.L. Russek, The evolution of magnetocaloric heat-pump devices, MRS Bull. 43 (2018) 274–279, https://doi.org/10.1557/mrs.2018.71.
[17] A. Smith, C.R.H. Bahl, R. Bjork, K. Engelbrecht, K.K. Nielsen, N. Pryds, Materials challenges for high performance magnetocaloric refrigeration devices, Adv. Energy Mater. 2 (2012) 1288–1318, https://doi.org/10.1002/aenm.201200167.
[18] D. Eriksen, K. Engelbrecht, C.R.H. Bahl, R. Bjørk, K.K. Nielsen, Effects of flow balancing on active magnetic regenerator performance, Appl. Therm. Eng. 103 (2016) 1–8, https://doi.org/10.1016/j.applthermaleng.2016.03.001.
[19] M. Masche, J. Liang, K. Engelbrecht, C.R.H. Bahl, Performance assessment of a rotary active magnetic regenerator prototype using gadolinium, Appl. Therm. Eng. 204 (2022), https://doi.org/10.1016/J.APPLTHERMALENG.2021.117947.
[20] D. Eriksen, K. Engelbrecht, C.R.H. Bahl, R. Bjørk, K.K. Nielsen, A.R. Insinga, N. Pryds, Design and experimental tests of a rotary active magnetic regenerator prototype, Int. J. Refrig. 58 (2015) 14–21, https://doi.org/10.1016/j.ijrefrig.2015.05.004.
[21] J.A. Barclay, W.A. Steyert, Active magnetic regenerator 4332135 (1982).
[22] A. Waske, M.E. Gruner, T. Gottschall, O. Gutfleisch, Magnetocaloric materials for refrigeration near room temperature, MRS Bull. 43 (2018) 269–273, https://doi.org/10.1557/mrs.2018.69.
[23] J. Liang, K. Engelbrecht, K.K. Nielsen, K. Loewe, H. Vieyra, A. Barcza, C.R.H. Bahl, Performance assessment of a triangular microchannel active magnetic regenerator, Appl. Therm. Eng. 186 (2021), 116519, https://doi.org/10.1016/j.applthermaleng.2020.116519.

[24] I. Batashev, Rational approaches to the design of magnetocaloric materials, Delft University of Technology, 2022. PhD thesis,.

[25] W. Brey, G. Nellis, S. Klein, Thermodynamic modeling of magnetic hysteresis in AMRR cycles, Int. J. Refrig. 47 (2014) 85–97, https://doi.org/10.1016/j.ijrefrig.2014.07.013.

[26] T. Lei, K. Engelbrecht, K.K. Nielsen, H. Neves Bez, C.R.H. Bahl, Study of multi-layer active magnetic regenerators using magnetocaloric materials with first and second order phase transition, J. Phys. D, Appl. Phys. 49 (2016), https://doi.org/10.1088/0022-3727/49/34/345001.

[27] F. Guillou, G. Porcari, H. Yibole, N. Van Dijk, E. Brück, Taming the first-order transition in giant magnetocaloric materials, Adv. Mater. 26 (2014) 2671–2675, https://doi.org/10.1002/ADMA.201304788.

[28] F. Guillou, H. Yibole, G. Porcari, L. Zhang, N.H. Van Dijk, E. Brück, Magnetocaloric effect, cyclability and coefficient of refrigerant performance in the MnFe(P, Si, B) system, J. Appl. Phys. 116 (2014) 63903, https://doi.org/10.1063/1.4892406.

[29] J. Lyubina, Magnetocaloric materials for energy efficient cooling, J. Phys. D. Appl. Phys. 50 (2017), https://doi.org/10.1088/1361-6463/50/5/053002.

[30] T. Gottschall, K.P. Skokov, M. Fries, A. Taubel, I. Radulov, F. Scheibel, D. Benke, S. Riegg, O. Gutfleisch, Making a Cool Choice: The Materials Library of Magnetic Refrigeration, Adv. Energy Mater. 9 (2019), https://doi.org/10.1002/aenm.201901322.

[31] R. Gauß, G. Homm, O. Gutfleisch, The Resource Basis of Magnetic Refrigeration, J. Ind. Ecol. 21 (2017) 1291–1300, https://doi.org/10.1111/JIEC.12488.

[32] M.A. Richard, A.M. Rowe, R. Chahine, Magnetic refrigeration: Single and multimaterial active magnetic regenerator experiments, J. Appl. Phys. 95 (2004) 2146–2150, https://doi.org/10.1063/1.1643200.

[33] A. Rowe, A. Tura, Experimental investigation of a three-material layered active magnetic regenerator, Int. J. Refrig. 29 (2006) 1286–1293, https://doi.org/10.1016/j.ijrefrig.2006.07.012.

[34] D.S. Arnold, A. Tura, A. Rowe, Experimental analysis of a two-material active magnetic regenerator, Int. J. Refrig. 34 (2011) 178–191, https://doi.org/10.1016/j.ijrefrig.2010.08.015.

[35] C. Archipley, J. Barclay, K. Meinhardt, G. Whyatt, E. Thomsen, J. Holladay, J. Cui, I. Anderson, S. Wolf, Methane liquefaction with an active magnetic regenerative refrigerator, Cryogenics (Guildf). 128 (2022), 103588, https://doi.org/10.1016/j.cryogenics.2022.103588.

[36] R. Teyber, P.V. Trevizoli, T.V. Christiaanse, P. Govindappa, I. Niknia, A. Rowe, Performance evaluation of two-layer active magnetic regenerators with second-order magnetocaloric materials, Appl. Therm. Eng. 106 (2016) 405–414, https://doi.org/10.1016/j.applthermaleng.2016.06.029.

[37] J. Tušek, A. Kitanovski, U. Tomc, C. Favero, A. Poredoš, Experimental comparison of multi-layered La-Fe-Co-Si and single-layered Gd active magnetic regenerators for use in a room-temperature magnetic refrigerator, Int. J. Refrig. 37 (2014) 117–126, https://doi.org/10.1016/j.ijrefrig.2013.09.003.

[38] P. Govindappa, P.V. Trevizoli, O. Campbell, I. Niknia, T.V. Christiaanse, R. Teyber, S. Misra, M.A. Schwind, D. Van Asten, L. Zhang, A. Rowe, Experimental investigation of MnFeP1-xAsx multilayer active magnetic regenerators, J. Phys. D. Appl. Phys. 50 (2017), https://doi.org/10.1088/1361-6463/aa7a33.

[39] K. Navickaitė, H.N. Bez, T. Lei, A. Barcza, H. Vieyra, C.R.H. Bahl, K. Engelbrecht, Experimental and numerical comparison of multi-layered La(Fe, Si, Mn)13Hy active magnetic regenerators, Int. J. Refrig. 86 (2018) 322–330, https://doi.org/10.1016/j.ijrefrig.2017.10.032.

[40] M. Masche, J. Liang, S. Dall'Olio, K. Engelbrecht, C.R.H. Bahl, Performance analysis of a high-efficiency multi-bed active magnetic regenerator device, Appl. Therm. Eng. 199 (2021) 117569. https://doi.org/10.1016/j.applthermaleng.2021.117569.

[41] T.V. Christiaanse, P.V. Trevizoli, S. Misra, C. Carroll, D. Van Asten, L. Zhang, R. Teyber, P. Govindappa, I. Niknia, A. Rowe, Experimental study of 2-layer regenerators using Mn-Fe-Si-P materials, J. Phys. D. Appl. Phys. 51 (2018), https://doi.org/10.1088/1361-6463/aaaba7.

[42] E. Brück, O. Tegus, D.T.C. Thanh, K.H.J. Buschow, Magnetocaloric refrigeration near room temperature (invited), J. Magn. Magn. Mater. 310 (2007) 2793–2799, https://doi.org/10.1016/j.jmmm.2006.10.1146.

[43] P. Govindappa, P.V. Trevizoli, I. Niknia, T.V. Christiaanse, R. Teyber, A. Rowe, Experimental characterization of multilayer active magnetic regenerators using first order materials: Multiple points of equilibrium, J. Appl. Phys. 124 (2018), https://doi.org/10.1063/1.5040491.

[44] T. Lei, K.K. Nielsen, K. Engelbrecht, C.R.H. Bahl, H. Neves Bez, C.T. Veje, Sensitivity study of multi-layer active magnetic regenerators using first order magnetocaloric material La(Fe, Mn, Si)13Hy, J. Appl. Phys. 118 (2015), https://doi.org/10.1063/1.4923356.

[45] Y. Li, G. Lin, J. Chen, Numerical investigation and performance evaluation of the MnFe-based composite magnetocaloric material with large magnetic entropy change over a wide temperature range, Int. J. Refrig. 121 (2021) 61–71, https://doi.org/10.1016/j.ijrefrig.2020.10.004.

[46] M. Zhang, O. Abdelaziz, A.M. Momen, A. Abu-Heiba, A numerical analysis of a magnetocaloric refrigerator with a 16-layer regenerator, Sci. Rep. 7 (2017) 1–12, https://doi.org/10.1038/s41598-017-14406-9.

[47] L. Yuan, S. Qian, J. Yu, Numerical study on the multi-layered magnetocaloric regenerators, Appl. Therm. Eng. 204 (2022), 118001, https://doi.org/10.1016/j.applthermaleng.2021.118001.

[48] M. Risser, P. Collet, J.-B. Chaudron, S. Lionte, C. Muller, Optimization of a layered regenerator inside a magnetocaloric cooling system using an evolutionary algorithm, in: Thermag VIII, 2018: pp. 120–125. https://doi.org/10.18462/iir.thermag.2018.0019.

[49] B. Monfared, B. Palm, Optimization of layered regenerator of a magnetic refrigeration device, Int. J. Refrig. 57 (2015) 103–111, https://doi.org/10.1016/j.ijrefrig.2015.04.019.

[50] H. Johra, K. Filonenko, P. Heiselberg, C. Veje, S. Dall'Olio, K. Engelbrecht, C. Bahl, Integration of a magnetocaloric heat pump in an energy flexible residential building, Renew. Energy. 136 (2019) 115–126. https://doi.org/10.1016/j.renene.2018.12.102.

[51] T.V. Christiaanse, P.V. Trevizoli, A. Rowe, Modelling two layer Mn–Fe–Si–P materials in an active magnetic regenerator, Int. J. Refrig. 106 (2019) 225–235, https://doi.org/10.1016/j.ijrefrig.2019.07.002.

[52] T. V. Christiaanse, An opensource active magnet regenerator model written in python, (2019). https://github.com/TheoChristiaanse/AMRmodel (accessed October 14, 2020).

[53] K.K. Nielsen, J. Tusek, K. Engelbrecht, S. Schopfer, A. Kitanovski, C.R.H. Bahl, A. Smith, N. Pryds, A. Poredos, Review on numerical modeling of active magnetic regenerators for room temperature applications, Int. J. Refrig. 34 (2011) 603–616, https://doi.org/10.1016/j.ijrefrig.2010.12.026.

[54] I. Niknia, O. Campbell, T.V. Christiaanse, P. Govindappa, R. Teyber, P.V. Trevizoli, A. Rowe, Impacts of configuration losses on active magnetic regenerator device performance, Appl. Therm. Eng. 106 (2016) 601–612, https://doi.org/10.1016/j.applthermaleng.2016.06.039.

[55] T.F. Petersen, N. Pryds, A. Smith, J. Hattel, H. Schmidt, H.J. Høgaard Knudsen, Two-dimensional mathematical model of a reciprocating room-temperature Active Magnetic Regenerator, Int. J. Refrig. 31 (2008) 432–443, https://doi.org/10.1016/J.IJREFRIG.2007.07.009.

[56] C. Aprea, A. Greco, A. Maiorino, C. Masselli, A comparison between rare earth and transition metals working as magnetic materials in an AMR refrigerator in the room temperature range, Appl. Therm. Eng. 91 (2015) 767–777, https://doi.org/10.1016/j.applthermaleng.2015.08.083.

[57] J. Tušek, A. Kitanovski, I. Prebil, A. Poredoš, Dynamic operation of an active magnetic regenerator (AMR): Numerical optimization of a packed-bed AMR, Int. J. Refrig. 34 (2011) 1507–1517, https://doi.org/10.1016/j.ijrefrig.2011.04.007.

[58] C. Aprea, A. Greco, A. Maiorino, Modelling an active magnetic refrigeration system: A comparison with different models of incompressible flow through a packed bed, Appl. Therm. Eng. 36 (2012) 296–306, https://doi.org/10.1016/j.applthermaleng.2011.10.034.

[59] D.J. Silva, J. Ventura, J.P. Araújo, Caloric devices: A review on numerical modeling and optimization strategies, Int. J. Energy Res. 45 (2021) 18498–18539, https://doi.org/10.1002/er.7023.

[60] A. Macias-Machin, L. Oufer, N. Wannenmacher, Heat transfer between an immersed wire and a liquid fluidized bed, Powder Technol. 66 (1991) (2021) 281–284, https://doi.org/10.1016/0032-5910(91)80041-G (accessed September 16.

[61] I. Park, Y. Kim, S. Jeong, Development of the tandem reciprocating magnetic regenerative refrigerator and numerical simulation for the dead volume effect, Int. J. Refrig. 36 (2013) 1741–1749, https://doi.org/10.1016/j.ijrefrig.2013.03.012.

[62] N. Wakao, S. Kaguei, Heat and mass transfer in packed beds, Gordon and Breach Science Publishers, 1982.

[63] M. Frischmann, K. Engelbrecht, G. Nellis, S. Klein, Heat Transfer Coefficient in a Packed Sphere Regenerator for use in Active Magnetic Regenerative Refrigeration, in: Int. Refrig. Air Cond. Conf., 2008: pp. 1–8. https://doi.org/http://docs.lib.purdue.edu/iracc/935.

[64] K.L. Engelbrecht, G.F. Nellis, S.A. Klein, The effect of internal temperature gradients on regenerator matrix performance, J. Heat Transfer. 128 (2006) 1060–1069, https://doi.org/10.1115/1.2345428.

[65] G.R. Hadley, Thermal conductivity of packed metal powders, Int. J. Heat Mass Transf. 29 (1986) 909–920, https://doi.org/10.1016/0017-9310(86)90186-9.

[66] S. Ergun, Fluid flow through packed columns, Chem. Eng. Prog. 48 (1952) 89–94.

[67] T. V. Christiaanse, Characterization, Experimentation and Modeling of Mn-Fe-Si-P Magnetocaloric Materials, University of Victoria, PhD thesis, 2018.

[68] P.V. Trevizoli, A.T. Nakashima, G.F. Peixer, J.R. Barbosa, Performance evaluation of an active magnetic regenerator for cooling applications - part I: Experimental analysis and thermodynamic performance, Int. J. Refrig. 72 (2016) 192–205, https://doi.org/10.1016/j.ijrefrig.2016.07.009.

[69] B. Huang, J.W. Lai, D.C. Zeng, Z.G. Zheng, B. Harrison, A. Oort, N.H. van Dijk, E. Brück, Development of an experimental rotary magnetic refrigerator prototype, Int. J. Refrig. 104 (2019) 42–50, https://doi.org/10.1016/j.ijrefrig.2019.04.029.

[70] B.P. Vieira, H.N. Bez, D. dos Santos, J.A. Lozano, J.R. Barbosa, Interrelationship between flow profiles and the magnetic waveform and their influence on the performance of first-order active magnetic regenerators, Appl. Therm. Eng. 219 (2023), 119581, https://doi.org/10.1016/J.APPLTHERMALENG.2022.119581.

[71] N.H. Dung, Z.Q. Ou, L. Caron, L. Zhang, D.T.C. Thanh, G.A. De Wijs, R.A. De Groot, K.H.J. Buschow, E. Brück, Mixed magnetism for refrigeration and energy conversion, Adv. Energy Mater. 1 (2011) 1215–1219, https://doi.org/10.1002/AENM.201100252.

[72] A.A. Kiss, C.A. Infante Ferreira, Heat Pumps in Chemical Process Industry, 2016. https://doi.org/10.1201/9781315371030.

[73] T. Lei, K. Engelbrecht, K.K. Nielsen, C.T. Veje, Study of geometries of active magnetic regenerators for room temperature magnetocaloric refrigeration, Appl. Therm. Eng. 111 (2017) 1232–1243, https://doi.org/10.1016/j.applthermaleng.2015.11.113.

[74] P.V. Trevizoli, A.T. Nakashima, G.F. Peixer, J.R. Barbosa, Performance assessment of different porous matrix geometries for active magnetic regenerators, Appl. Energy. 187 (2017) 847–861, https://doi.org/10.1016/j.apenergy.2016.11.031.